POLITECNICO DI TORINO

Faculty of Engineering
Master of Science in Aerospace

Master's Thesis

Vibrissa-shaped cylinder as passive noise control

Supervisors:
Prof. Francesco Avallone
Prof. Beckett Zhou
Dr. Mario Ali

Candidate:
Riccardo Martellucci

Abstract

The following research project aims to investigate the aeroacoustics properties of a vibrissa-shaped cylinder. This bio-inspired geometry is modeled after the whiskers of harbour seals. Initial researches on the properties of these whiskers have revealed their adaptive ability to suppress the vortex shedding. Vortex shedding is a fluid dynamic phenomenon associated with a bluff body, such as a circular cylinder, in cross-flow. The formation of vortex shedding generates aerodynamic noise, which is the primary focus of the following study. Specifically, the aerodynamic noise produced by both geometries is evaluated and compared to validate findings from literature regarding the vibrissa-shaped cylinder's capability to reduce noise levels compared to a circular cylinder. Numerical investigations delve into the reasons for this reduction, with a particular emphasis on the distinct wake pattern of the vibrissa-shaped cylinder in the absence of vortex shedding.

List of Tables

List of Figures

Contents

Chapter 1

Introduction

1.1 Experience and research abroad

This research project commenced in October 2023 with a period of work abroad at the *University of Bristol* in England, under the supervision of Professor *Beckett Zhou*. Although the time spent at the *University of Bristol* did not yield the initially anticipated results, it was instrumental for the work conducted upon my return to Italy at the *Politecnico di Torino* under the supervision of Professor *Francesco Avallone*. The opportunity to work abroad allowed me to engage with the world of research, particularly numerical research, for the first time. I interacted with a group of researchers and PhD students who guided me and integrated me into the research environment.
From the standpoint of knowledge specific to the thesis work, my time at Bristol was equally beneficial. I had the chance to learn mesh generation using the *Pointwise* mesh generator tool. This experience enabled me to critically evaluate the mesh generation implemented with *PowerFLOW*, the software subsequently used at the *Politecnico di Torino*. Additionally, at the *University of Bristol*, an initial try involved resolving the flow field using the SU^2 software with a large-eddy approach. Although the simulations did not produce the desired results, they provided me with the opportunity to evaluate my first fluid dynamics results and enhance my ability to critically assess them. The insights gained were crucial for the results obtained at the *Politecnico di Torino*, which are presented in Chapter 4. My prior knowledge of the fluid-dynamics patterns and evaluation techniques significantly aided in understanding the simulation status, assessing its reliability, and commenting on the results obtained.

1.2 State of the art

This thesis aims to investigate the aeroacoustics performance of a new bio-inspired geometry, called a vibrissa-shaped cylinder, in terms of its capability to reduce the noise level of a circular cylinder.
This first chapter presents the state of the art in terms of knowledge of physical phenomena and engineering implications. The background scenario is that of bluff bodies in cross-flow, i.e., in the normal direction to the upstream flow. The resulting fluid-dynamic wake downstream of the bluff bodies is responsible for significant noise levels in several applications, such as aircraft landing gear [24]. One of the most studied bodies is the circular cylinder; it exhibits a well-known behaviour that depends on the values of the Reynolds number. During the 20th century, many studies were conducted on the fluid dynamics of the cylinder and its role as a source of aeroacoustic noise. These studies are reviewed by *D. Sumner* in [8] and by *R.D. Blevins* in [4]. Given the context, what is of interest is the field of flow control to modify the wake pattern to control the noise and thus reduce the sound level, which will be detailed in Section 1.2.2.

Attenuating the sound level means reducing the noise level, which is the aim of many recent studies, as noise control has become a crucial point, for example, in aviation regulations [10].

1.2.1 Circular cylinder in cross-flow

After presenting the scenario of interest, it is appropriate to describe the physical phenomenon associated with a cylindrical bluff body, which is the classical example of a two-dimensional bluff body (under low-velocity conditions) in cross-flow, as shown in Figure 1.1. In aerodynamics, bluff bodies are defined as bodies that, as a result of their shapes, have separated flow over a substantial part of their surfaces. The phenomenon has been thoroughly described in the literature and studied over the last century by *Marris* [23], *Kovásznay* [18], *Tritton* [33], *Schaefer and Eskinazi* [29], *Roshko* [28], and *Lienhard* [20].
The seemingly straightforward circular cylinder exhibits intricate fluid dynamics under steady mean flow conditions, characterized by the formation of two distinct free shear layers, the alternating generation of spanwise vortices in its near-wake zone, and a wake that manifests as highly turbulent and three-dimensional. These vortices are periodically shed, creating two parallel rows of vortices with opposing spins, forming a Kármán vortex street. Each of these features is shown in Figure 1.2 and can be observed for most flow regime conditions, which will be described later. When the cylinder is immersed in a cross-flow of uniform free-stream velocity (U), the axis is oriented with the mean flow direction, and the y- and z-axes are in mutually perpendicular transverse and spanwise directions, respectively.
When a circular cylinder moves in a fluid medium (or conversely, when the fluid passes through the cylinder, according to Newton's third law), it disrupts the gas molecules in its vicinity, causing them to circulate around the object. This leads to the generation of aerodynamic forces between the gas and the object, the magnitude of which depends on various factors. These factors include the shape of the object, its velocity, the mass of the passing gas and two key properties of the gas: its viscosity and compressibility. Under low Mach number conditions, compressibility effects are generally negligible. To accurately include these effects, aerodynamicists use similarity parameters, of which Reynolds number is particularly important. The Reynolds number expresses the ratio of inertial (resistant to change or motion) forces to viscous forces. From a detailed analysis of the momentum conservation equation, the inertial forces are characterised by the product of the density (ρ) times the velocity (V) times the gradient of the velocity ($\frac{dV}{dx}$). The viscous forces are characterised by the dynamic viscosity coefficient (μ) times the second gradient of the velocity ($\frac{d^2V}{dx^2}$). The Reynolds number (Re) then becomes:

$$Re = \frac{\text{Inertia force}}{\text{Viscous force}} = \frac{\rho V \frac{dV}{dx}}{\mu \frac{d^2V}{dx^2}} = \frac{\rho V \frac{V}{L}}{\mu \frac{V^2}{L^2}} = \frac{\rho V L}{\mu} \tag{1.1}$$

The Reynolds number is a dimensionless number.

The fluid pattern associated depends on different Reynolds numbers, i.e., the balance of the two forces, and six different regimes can be identified (as shown in Figure 1.3). However, the number of regimes and their definitions typically differ from study to study, as do the Reynolds number boundaries. For example, seven regimes are identified in *D. Sumner*'s review [8].

Very Low Reynolds Numbers

At Reynolds numbers below Re < 5, the flow pattern around the cylinder exhibits symmetry and stability, with adherence to the cylinder's surface. This state is often denoted as the Stokes regime, characterised by a predominant influence of viscous forces and the presence of laminar fluid behaviour. Streamlines near the cylinder run parallel to its surface, encompassing it entirely. Notably, two stagnation points emerge-one upstream at 0° and another downstream at 180°—with no separation occurring over the circular section [8].

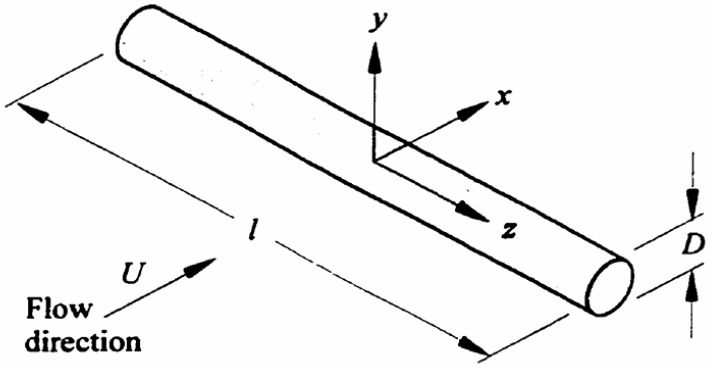

Figure 1.1: Circular Cylinder in Cross-Flow [8]

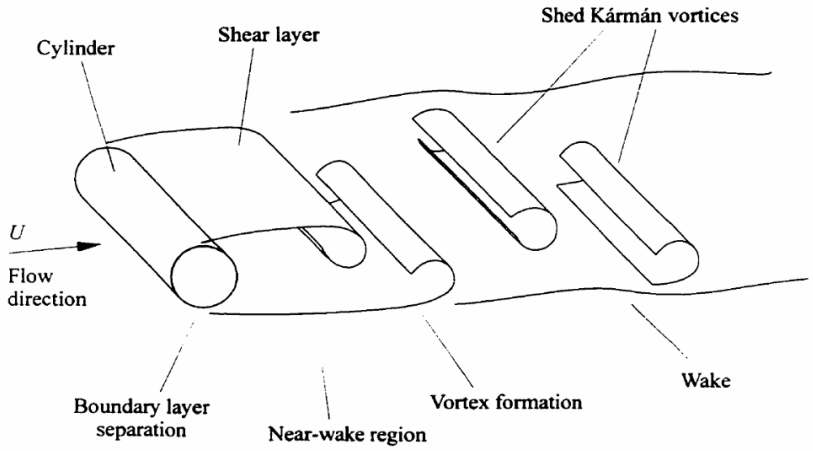

Figure 1.2: Periodic, alternate vortex shedding from a circular cylinder in steady cross-flow, at subcritical Reynolds numbers [8]

In the range $5 \leq \mathrm{Re} \leq 40$, a distinct flow regime emerges. In this case, the flow detaches from the cylinder surface, leading to the formation of two distinct shear layers that encapsulate a recirculation zone within the near-wake region. This zone contains a pair of stationary vortices with equal intensity but opposite directions of rotation. Initially, the separation begins near the downstream stagnation point and gradually progresses forward along the cylinder surface as the Reynolds number increases, resulting in the expansion of the recirculation zone [8].

Laminar Vortex Shedding

At $\mathrm{Re} = 40$, a significant transition occurs, marking the onset of the described features in the previous Section 1.2.1. As the Reynolds number increases, the recirculation zone and its accompanying pair of stationary eddies begin to disintegrate, initiating periodic vortex generation and shedding in the wake of

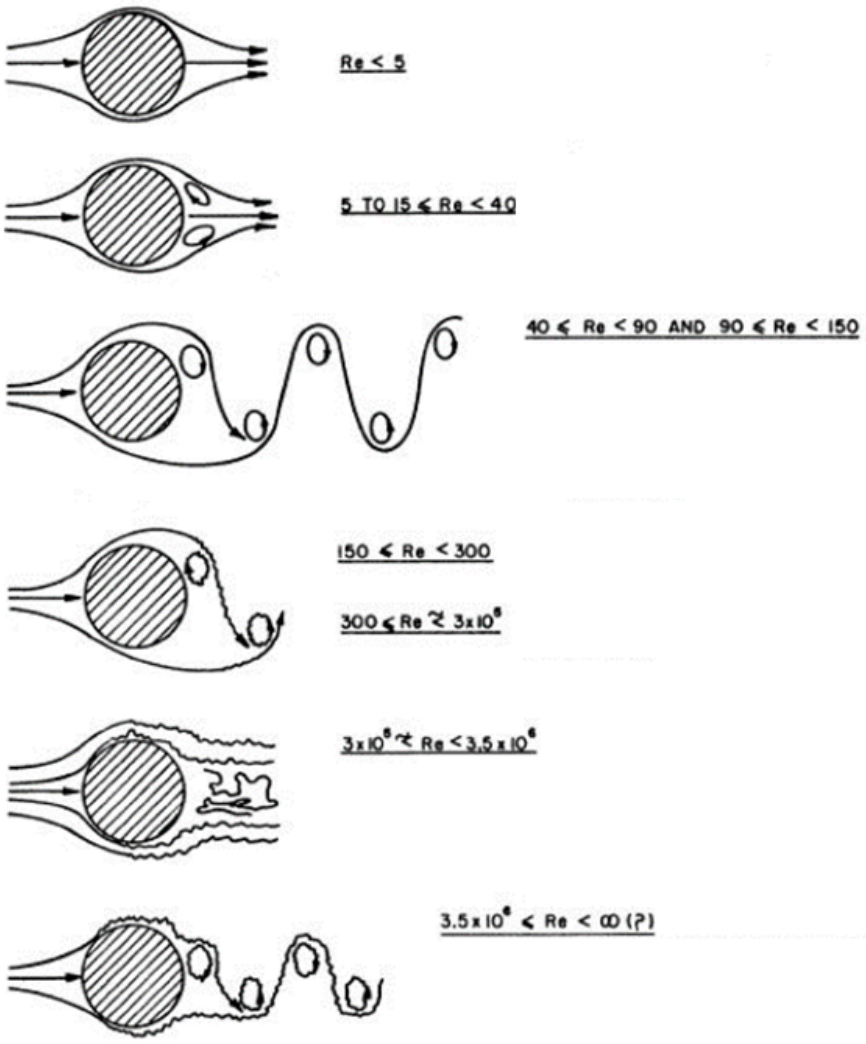

Figure 1.3: Flow across a cylinder over a different number of Reynolds [20]

the cylinder. This process leads to the formation of a Kármán vortex street. Primary vortices, known as Kármán vortices, are shed alternately from the two separated free shear layers. Instabilities within the recirculation zone may result in the detachment of one of the stationary eddies from the cylinder. The previously confined shear layers, which previously enclosed the recirculation zone at lower Reynolds numbers, now become unrestricted, exhibiting an alternating rolling motion from one side of the cylinder to the other. This motion generates vortices of opposite sign. Each vortex is shed into the wake of the cylinder in a consistent alternating pattern, creating a regular arrangement of two rows of vortices with opposite signs, forming the characteristic Kármán vortex street. It's noteworthy that this wake pattern remains fully laminar [8].

Subcritical Flow

In a first range of Reynolds numbers, $150 \leq \mathrm{Re} < 300$, the transition to turbulence in the vortex street can be identified. The Kármán vortices become increasingly turbulent, boundary layer separation exhibits

spanwise nonuniformities, and the free shear layers become increasingly unstable with the formation of transition waves and shear layer instability vortices [8]. For $\mathrm{Re} > 300$, in a range of $300 \leq \mathrm{Re} < 3 \times 10^5$, a fully turbulent vortex street is established. Laminar separation of the boundary layers (before transitioning to turbulence) occurs at almost 90° from the forward stagnation point throughout the subcritical regime, and Kármán vortex shedding occurs at a nearly constant value of the Strouhal number, close to $\mathrm{St} = 0.2$. This non-dimensional parameter will be detailed later.

Critical, Supercritical and Post-Critical Flow

In the critical flow regime ($\mathrm{Re} = 3 \times 10^5$), the boundary layer initially separates in a laminar state and then reattaches turbulently. This flow behaviour is depicted in Figure 1.4. The transition to turbulence takes place within a separation bubble on the cylinder's surface [8]. Up to $\mathrm{Re} = 3 \times 10^5$, the inertial forces dominate, effectively counteracting the adverse pressure gradient on the circular section due to the high energy characteristics of the flow. This causes the separation point to move further downstream, approximately at 120°. From near the upstream stagnation point, the cylinder's boundary layer becomes fully turbulent, and organised vortex shedding begins again. In this wake pattern, vortex shedding is diffused, and the shedding frequency should be defined as the dominant frequency within a spectrum of component frequencies, rather than as the frequency of alternating emission of vortices above and below [20]. As a result, the boundary layer experiences final turbulent separation, leading to a narrower cylinder wake.

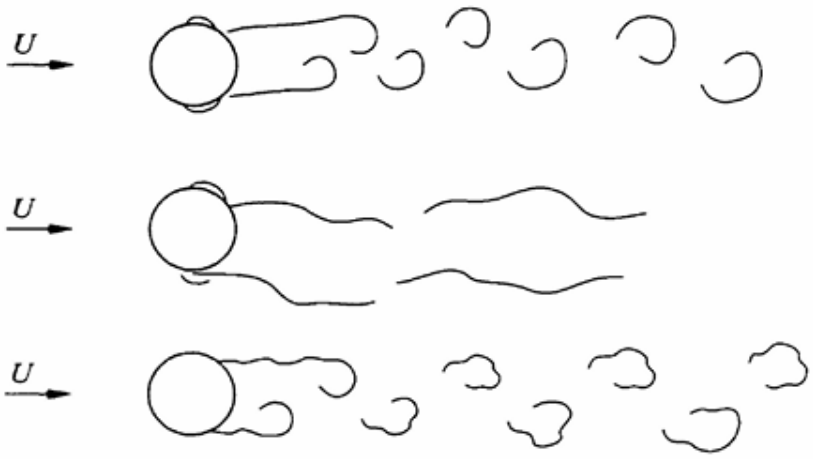

Figure 1.4: Critical regime, supercritical regime, post-critical regime

As previously mentioned, in Section 1.2.1, the Strouhal number is another characteristic and necessary non-dimensional parameter to describe vortex shedding. It is strictly related to the shedding frequency (f_s), i.e., the frequency of the alternating up-and-down emission of vortices or, at the highest values of Reynolds number, the dominant frequency in the spectrum. The Strouhal number (St) is mathematically expressed as:

$$St = \frac{f_s D}{U} \tag{1.2}$$

where D is the diameter of the cylinder and U is the free-stream velocity. It describes oscillating flow mechanisms and aims to express the ratio of inertial forces resulting from the local acceleration of the flow

to those arising from the convective acceleration. [17]. The presence of the free stream velocity between the Reynolds number and the Strouhal number leads to a relationship between the two parameters. Several empirical and semi-empirical formulae for the *St-Re* relationship over certain ranges of Reynolds number were proposed, for example:

$$(1) \quad St = A + \frac{B}{Re} \quad \text{by} \quad Roshko[28] \tag{1.3}$$

$$(2) \quad St = A + \frac{B}{\sqrt{Re}} \quad \text{by} \quad Fey\ et\ al[11] \tag{1.4}$$

where A and B are curve-fitting coefficients. These formulae are often applicable for low Reynolds number cases. However, it might be better to refer to the graph by *Lienhard* [20], which reports existing data showing the relationship between St and Re over a wide range of Reynolds numbers, as shown in Figure 1.5. In this fluid dynamics scenario, another phenomenon is strictly related, and what is described above

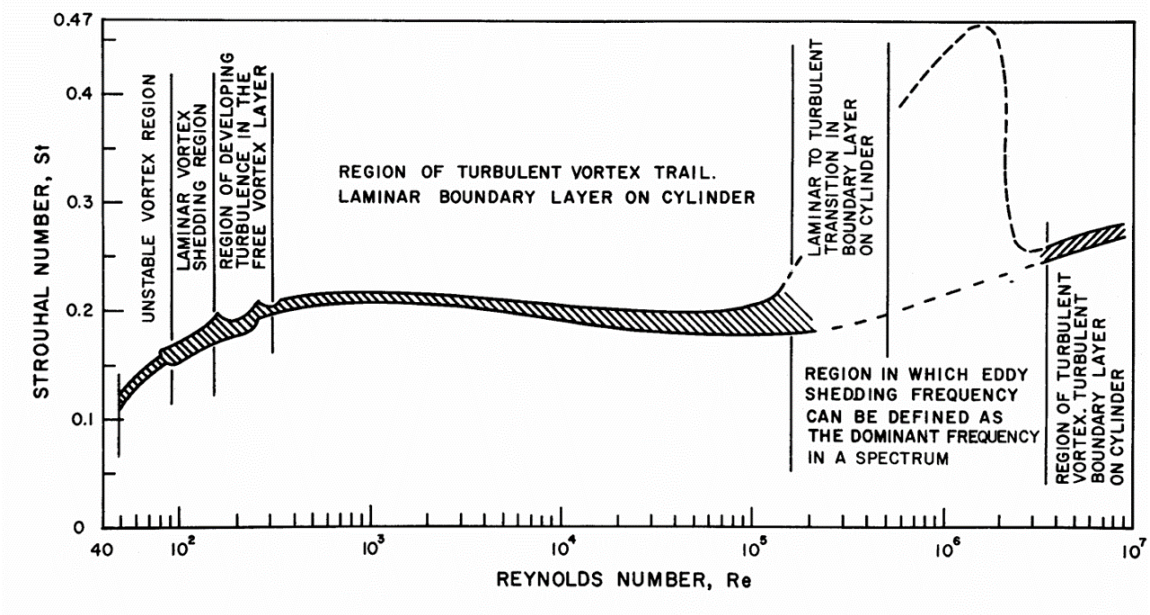

Figure 1.5: The Strouhal-Reynolds number relationship for circular cylinders [20]

represents the causes; this is the aeroacoustic phenomenon called aeolian tone [25], [27].

1.2.2 Aeolian tone

The Aeolian tone, a nearly pure tone sound, exemplifies aerodynamic noise and is a monotonous aerodynamic phenomenon generated by Kármán vortex shedding in the wake of two-dimensional cylinders [12]. This phenomenon has been recognised for a long time. For instance, in 1956, *Phillip*s [25], using Curle's aerodynamic sound theory, attempted to predict the Aeolian tone for Reynolds number Re < 160. Moreover, *Lighthill* established a solid foundation for aerodynamic sound theories in 1952 [21] through his study of jet engine noise. He treated aerodynamic sound as a by-product of fluid motion and introduced the concept of acoustic analogy. Specifically, he examined the sound field produced by the unsteady motion of an unbounded fluid, facilitating the study of noise generation by turbulent fluid flow. In 1955, *Curle* [7] expanded *Lighthill*'s solution by incorporating the effect of solid boundaries, enhancing the understanding of the Aeolian tone. The aim of *Curle*'s paper [7] is to evaluate the effects of solid boundaries that manifest in two ways:

1. Sound due to the reflection and diffraction of quadrupoles given by Lighthill's theory related to turbulent acoustic source.

2. Through a distribution of dipoles at the boundaries, linked to the forces between the fluid and the solid boundary.

It follows that the solution is the sum of the volume integral given by Lighthill's solution and a surface integral along the solid boundaries. The surface integral represents modifications to Lighthill's theory necessitated by the presence of solid boundaries, which exactly amounts to the sound generated by a distribution of dipoles representing the fluctuating forces with which the solid boundaries act on the flow. Thus, the sound field can be considered as derived from two distinct sources [7]:

1. A Quadrupole field representing the fluctuating applied stresses.

2. A Dipole field representing the fluctuating force with which the solid boundaries act on the fluid.

Furthermore, from a dimensional analysis, it follows that the dipole contribution is dominant as the Mach number decreases. Additionally, it is demonstrated that the fluctuating force exerted on the fluid at the solid boundaries will have the same frequency as the velocity frequencies. Substantially, the fundamental result of his paper is [7]:

$$\rho - \rho_0 = \frac{1}{4\pi a_0^2}\frac{\partial^2}{\partial x_i \partial x_j}\int_V \frac{T_{ij}(\vec{y}, t - \frac{r}{a_0})}{r} d\vec{y} - \frac{1}{4\pi a_0^2}\frac{\partial}{\partial x_i}\int_S \frac{P_i(\vec{y}, t - \frac{r}{a_0})}{r} dS(\vec{y}); \tag{1.5}$$

where r is the distance from the centre of the surface to the sound observation point, a_0 is the speed of sound and $t - \frac{r}{a_0}$ is the retarded time. However, $T_{ij} = \rho v_i v_j + p_{ij} - a_0^2 \rho \delta_{ij}$ is the Lighthill stress tensor and $P_i = -l_j p_{ij}$ is exactly the force per unit area exerted on the fluid by the solid boundaries in the x_i direction [7]. Thus, physically the sound field could be seen as the sum of that generated by a volume distribution of quadrupoles and by a surface distribution of dipoles [7].
Therefore, a typical acoustic spectrum for the circular cylinder shows the presence of Aeolian tones as noise peaks around the frequency associated with lift fluctuations, followed by lower noise level peaks at subsequent harmonics, i.e., at discrete jumps of the frequency value associated with lift fluctuations, for example, 2 times. It is shown in Figure 1.6 an example of it for a Reynolds number of 76,600 from literature[9]. Our study fits within what has been presented so far. We are numerically computing a steady and rigid circular cylinder in a low Mach air stream in cross-flow, i.e., the cylinder is located perpendicular to the direction of the flow, at a Reynolds number of 37000. The Reynolds number value has been chosen in line with the benchmark results from numerical and experimental research on a circular cylinder and a vibrissa-shaped cylinder by *Smith*, *Chen*, and *Zang* [30].

Flow control

To reiterate the point made earlier, in Section 1.2 , reducing sound levels can be effectively achieved through flow control techniques. The ability to manipulate a flow has important engineering implications. These methods are commonly employed to delay transition, reduce drag, enhance lift, or suppress noise. Flow control can be categorised into active or passive types. Active flow control involves altering the flow structure with energy inputs, while passive flow control involves changing the geometry. Geometry modification changes the surface shape to alter the near-wall flow structures and reduce flow-induced noise and it is easy to implement. Many studies examined different shapes from the circular one, such as wavy-shaped, elliptical shape, and square shape [3, 1, 31, 2]. These studies indicate that altering

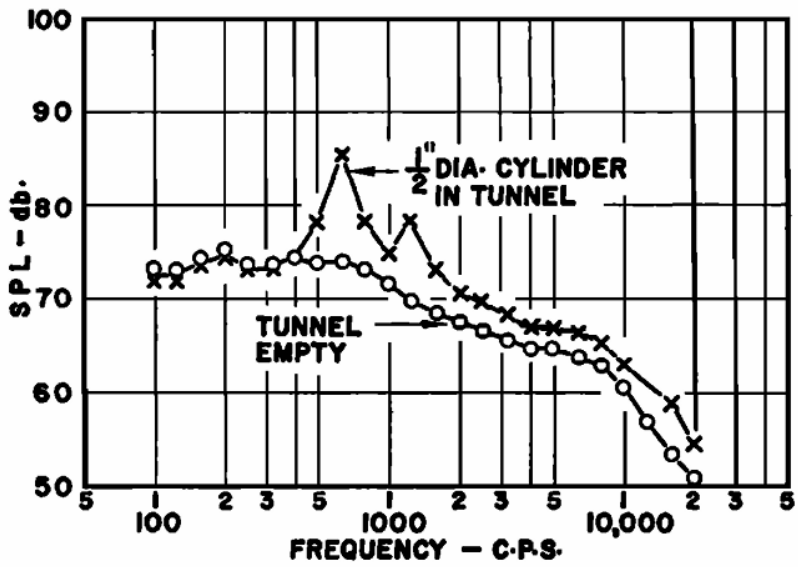

Figure 1.6: Spectrum of cylinder noise [9]

the geometry can impact the dynamics of flow separation from the circular cylinder, thereby modifying near-wake flow structures and vortex-shedding behaviour. For instance, elliptical cylinders produce smaller and weaker vortices due to their reduced windward area compared to circular cylinders [34]. In this context, biologically inspired geometries show significant potential for noise control, as evolutionary adaptations in species often lead to structures with beneficial capabilities. The vibrissa-shaped cylinder studied here is inspired by the shape of the whiskers (or vibrissae) of the harbour seal (*Phoca vitulina*), as depicted in Figure 1.7 [13].

Figure 1.7: Structure of harbour seal (*Phoca vitulina*) [13]

1.2.3 Vibrissa-shaped cylinder in cross-flow

Harbour seals' whiskers exhibit complex three-dimensional geometries that vary among different species. Generally, their morphology can be described as an elliptical cylinder with a wavy surface along the two edges. These undulations are out of phase, resulting in the two maximum and minimum points being located at different positions along the edges. This variation along the span direction contributes to the three-dimensional characteristic.The initial numerical and parametric definition, crucial for engineering implementation, was provided by Hanke et al. [13]. They extracted and averaged values from real vibrissae, establishing an initial model with seven geometrical parameters, as depicted in Figure 1.8. Further discussion on the vibrissa will be presented below, offering a more detailed description in Chapter 2. The specification of the vibrissa-shaped cylinder necessitates values for the major and minor semi-axes of the maximum ellipse (a and b), the major and minor semi-axes of the minimum ellipse (k and l), the distance between the two ellipses (M), and the two offset angles. These angles, denoted as the orientation angles of the major axis relative to the vibrissal axis, are α and β, respectively, for the maximum and minimum ellipse.

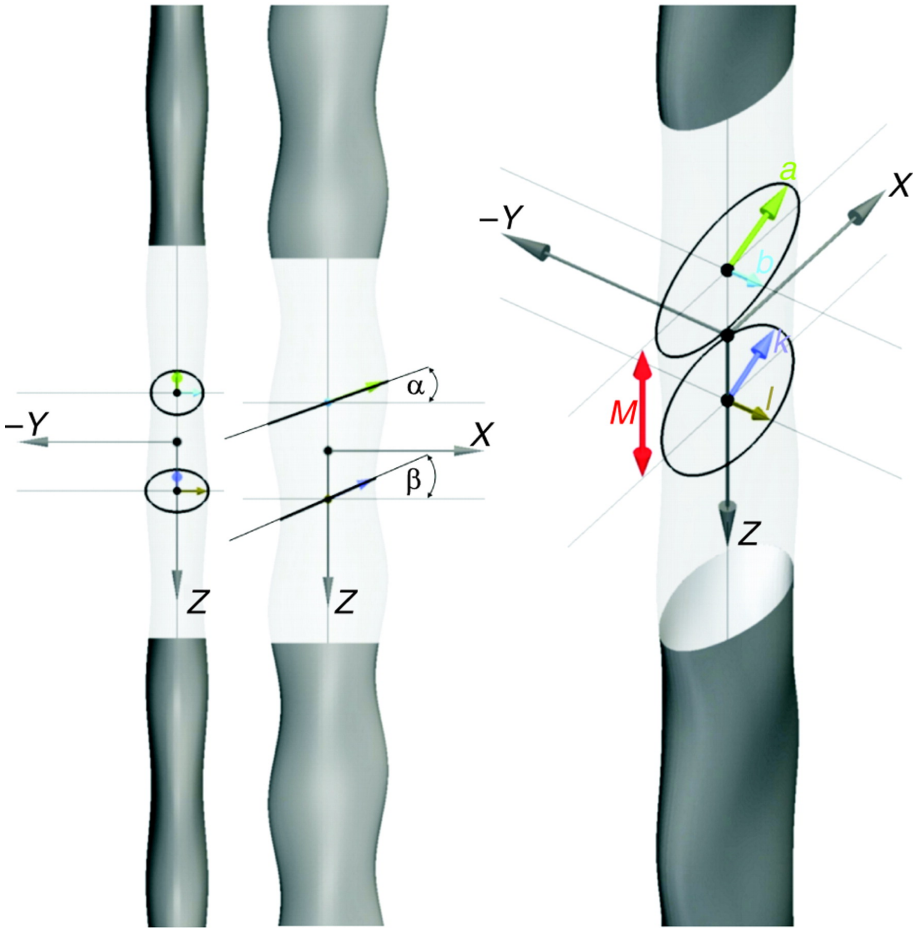

Figure 1.8: Vibrissa geometry [13]

Thus, once a model of the geometry is defined using the 7 featured parameters, the fluid dynamics behind it can be evaluated in depth through experimental or numerical simulations.
Initial experimental and numerical investigations have revealed a reduction in vortex-induced vibrations (VIVs) [13], commonly observed in objects moving through water and closely linked with vortex shedding.

In bluff bodies, where this phenomenon prevails, various forms of induced vibrations can be identified (e.g., forced-induced vibrations by Kármán vortex shedding or synchronisation accompanied by Kármán vortex street [16]), all inherently associated with vortex shedding. Moreover, *Hanke et al.* [13] found that the suppression of VIVs, and consequently of vortex shedding, can be attributed to the unique morphology of the vibrissae. Consequently, an analysis of lift and drag fluctuations, direct consequences of vortex shedding due to pressure field fluctuations, reveals a substantial reduction in both lift and drag fluctuations for vibrissae compared to a circular cylinder [13, 35, 6, 30], as depicted in Figure 1.9 from the study by *Hanke et al.* at $\mathrm{Re} = 500$. To show its wake pattern it is necessary to define how to interpret its

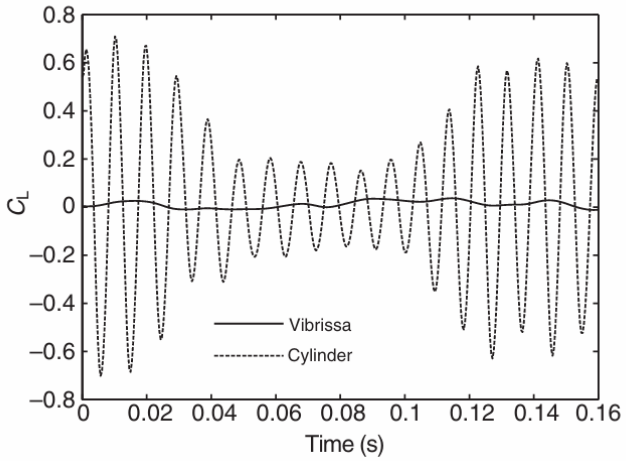

(a) Time-history of the lift coefficient

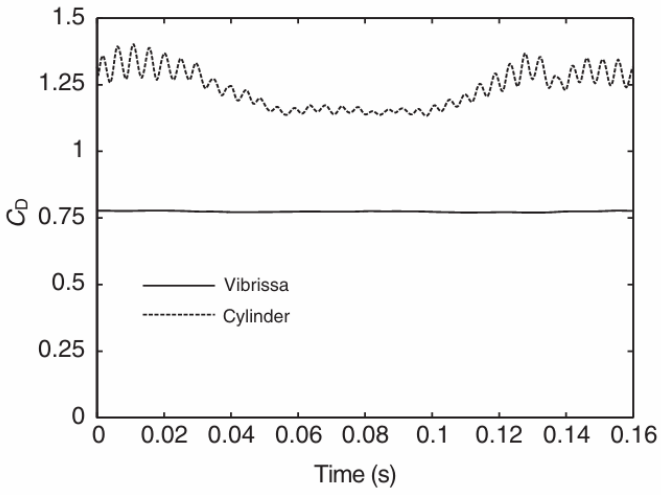

(b) Time-history of the drag coefficient

Figure 1.9: Lift and drag coefficients from a circular cylinder and a vibrissa [6]

fluid dynamics; to do this, two distinctive points are used: the nodal point and the saddle point, i.e., the point of maximum and minimum curvature along the trailing edge of the model. From these two points pass the two horizontal planes under analysis, which bear the same name; they can be seen in Figure 1.8. For a bluff body, it is sufficient to study the behaviour behind the horizontal plane (the plane in

the stream and longitudinal directions) to assess vortex shedding; whereas, for the vibrissae, a vertical plane (the plane in the span and stream directions) is necessary due to its three-dimensionality. From this perspective, what happens for the vibrissa is characterised by different behaviours compared to the nodal and saddle planes. Investigating in depth the fluid dynamics wake pattern behind the vibrissa and its causes, complex 3D dynamics have been discovered, implying and leading to completely different vortical structures in the vibrissa's wake. An important contribution to the evaluation and explanation of the fluid-dynamic phenomena involved in a vibrissa-shaped cylinder in cross-flow has been given by *Wang* and *Liu* [34] in 2016. The recent year of publication of the research explains how the topic is of current interest and how not all the reasons and fluid-dynamic implications are yet known; what is now outlined is a summary of what is known and especially what is clearly evident in relation to different wake behaviour between a vibrissa-shaped cylinder and a circular cylinder. The wake pattern for a vibrissa is assessed at $Re = 1800$, revealing markedly distinct behaviour compared to a circular cylinder. Specifically, the wake behind the vibrissa-shaped cylinder exhibits a significantly reduced recirculation zone and a highly stable reversed flow. This disparity arises from their differing upwind areas, resulting in distinct recirculation zones. Notably, the nodal recirculation zone is smaller both in the streamwise direction and longitudinally. Thus, compared to the circular cylinder show a change in the wake pattern [34], as shown in Figure 1.10. Indeed, the recirculation zone is certainly smaller, even in the saddle plane, for

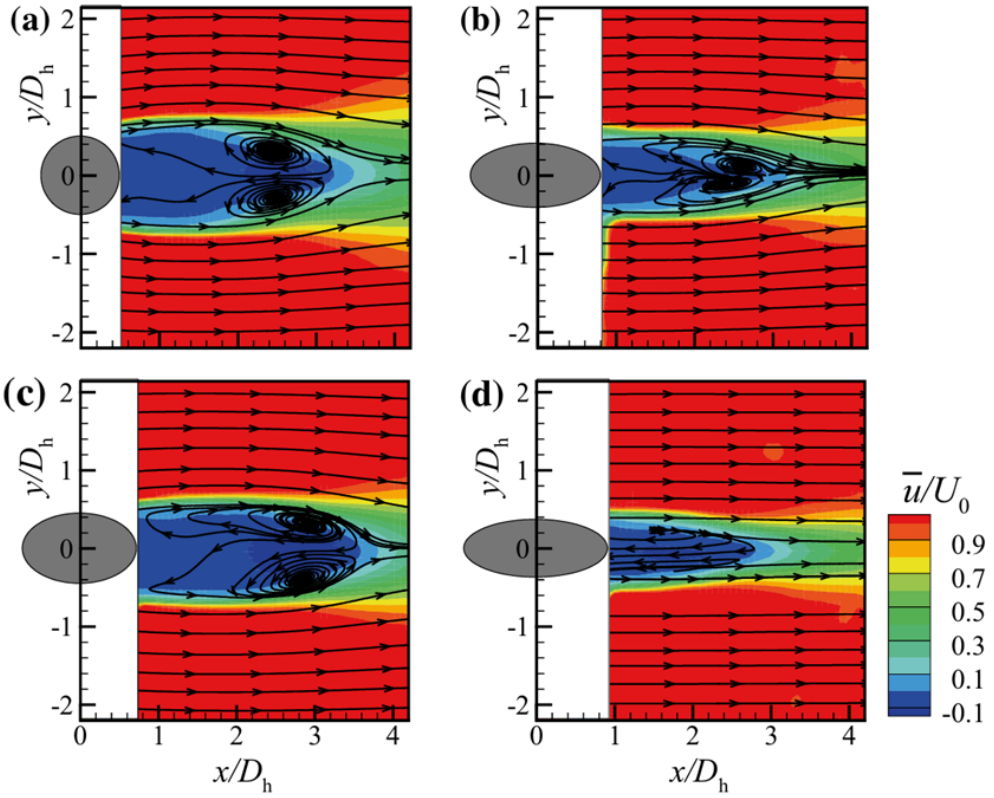

Figure 1.10: Streamline pattern and contour plot of time-averaged streamwise velocity in the horizontal plane, in order: a) Circular Cylinder, b) Elliptical Cylinder, c) Vibrissa-Shaped Cylinder (*saddle plane*), d) Vibrissa-Shaped Cylinder (*nodal plane*), [34]

the vibrissa than for the circular cylinder, but very important is the great difference in the strength (in Figure 1.11) and correlation of the unstable events. The unstable events for the vibrissa are poorly

organised by sequence and significantly limited in their spatial extent, as shown in Figure 1.12 [34].

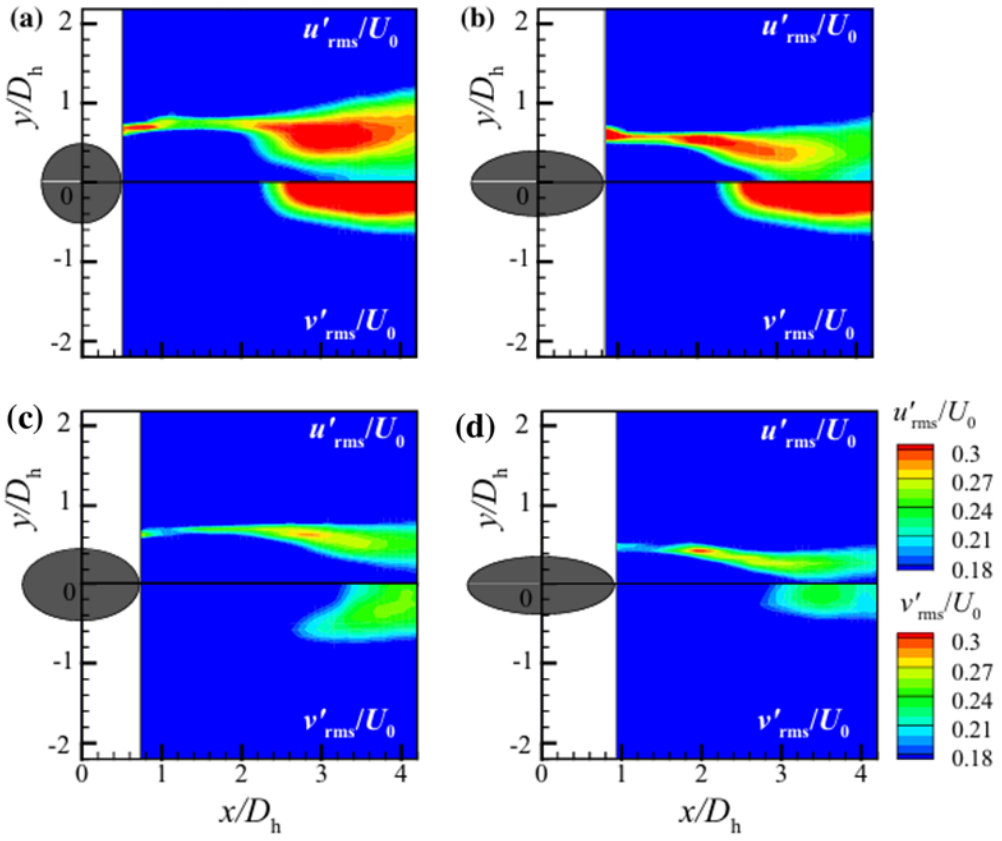

Figure 1.11: Contour plot of the streamwise and longitudinal velocity fluctuation intensities, in order: a) Circular Cylinder, b) Elliptical Cylinder, c) Vibrissa-Shaped Cylinder (*saddle plane*), d) Vibrissa-Shaped Cylinder (*nodal plane*) [34]

The rationale behind this phenomenon can be attributed to the complex three-dimensional structure and the presence of two distinct offset angles. Furthermore, there is a lateral motion of the nearby fluid along the span of the structure, leading to disruptions in the formation of vortical patterns typically associated with vortex shedding. Another notable observation stems from the examination of dominant modes at $St = 0.23$ and $St = 0.3$, which were found to be located in the saddle and nodal planes of the vibrissa-shaped cylinder system, respectively, that can interact with the spanwise motion in the distortion and disruption of vortices. The significant reduction in streamwise and longitudinal velocity fluctuation intensities indicates a substantial suppression of the vortex shedding process, contributing to a reduction in fluctuating forces on the cylinder. Consequently, due to its unique geometry, the vibrissa-shaped cylinder disrupts vortex formation and impedes vortex shedding [34, 15]. This new fluid-dynamic scenario seems to yield important results in noise control. In fact, the above fluid dynamics behaviour for a vibrissa-shaped cylinder in cross-flow, and so, the suppression in the rising of a clear, distinct, regular vortex shedding, as in the circular cylinder, has aeroacoustic implication in terms of the theory of sound which bases the level on noise on the force fluctuations associated to the vortex shedding. In fact, what is clearly shown by *Smith*, *Chen* and *Zang* [30] (also in [5] and [22]) is a completely different acoustic spectrum for a vibrissa cylinder than for a circular cylinder, as shown in Figure 1.13. It is easy to see the absence of the aeolian tones corresponding to the first highest peak in terms of level of noise at the value of the frequency of

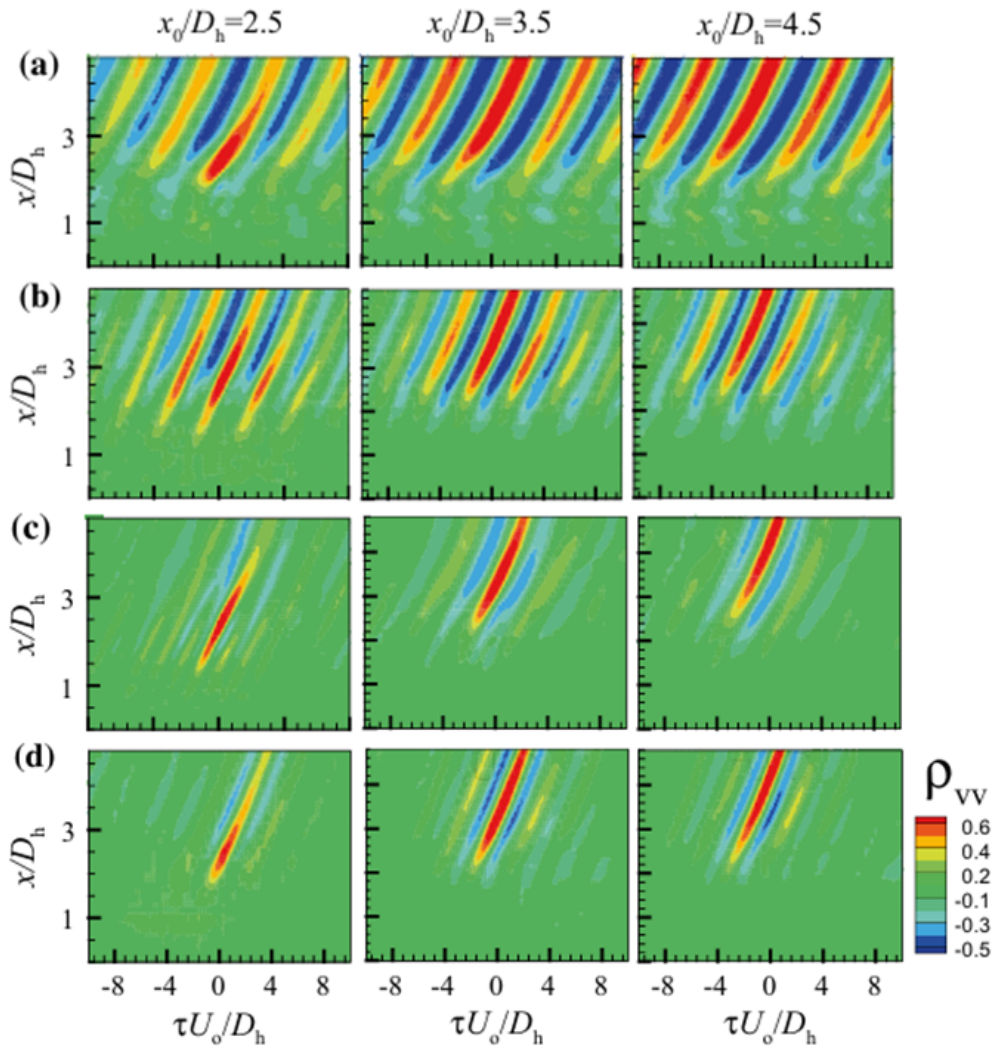

Figure 1.12: Cross-correlation of the fluctuating longitudinal velocity at different reference stations in the horizontal plane, in order: a) Circular Cylinder, b) Elliptical Cylinder, c) Vibrissa-Shaped Cylinder (*saddle plane*), d) Vibrissa-Shaped Cylinder (*nodal plane*) [34]

shedding and the second harmonic at the value of double value of the frequency of shedding. Moreover, all over the frequency spectrum the level of noise is reduced. This global view on vibrissa-shaped cylinder unique aeroacoustic behaviour in terms of reduced level of noise is of high interest in the corresponding field and in this scenario is put the present research.

1.3 Scope of this work

The above global view of the unique aeroacoustic behaviour of the vibrissa-shaped cylinder, in terms of noise reduction, is of great interest in the corresponding field. In this scenario, the present research aims to study the aeroacoustic performance of the vibrissa in relation to that of a circular cylinder, seeking to interpret the aeroacoustic results through the different fluid dynamics of the vibrissa. Therefore, to ensure a close comparison with benchmark results, the same geometry for the circular cylinder and the vibrissa-shaped cylinder, presented in Chapter 2, has been chosen. Additionally, to work in fluid-dynamic

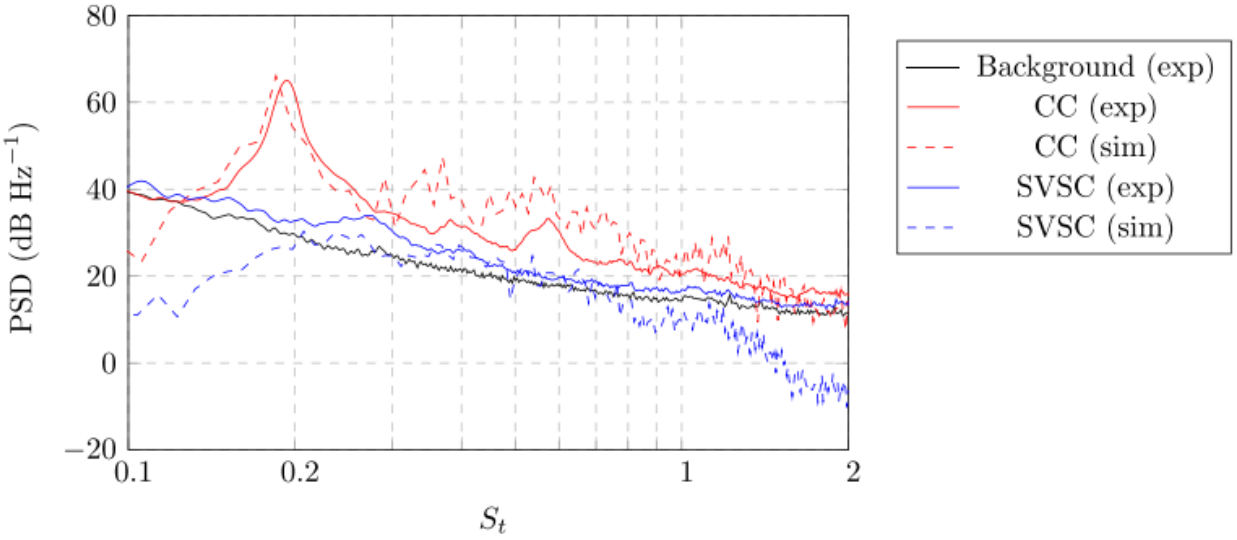

Figure 1.13: PSD spectrum of SPL [30]

similarity, the same Reynolds number (Re = 37000) has been selected.

Chapter 2

Geometry Configurations

2.1 Circular Cylinder

As mentioned in the previous chapter, a circular cylinder (CC) is used in the present research as a baseline. Its geometrical parameters are consistent with the configuration proposed and used in benchmark research [30]. The values are reported in Table 2.1, where a span length (L) of 10 times the diameter (D) has been chosen. The cylinder is shown in Figure 2.1.

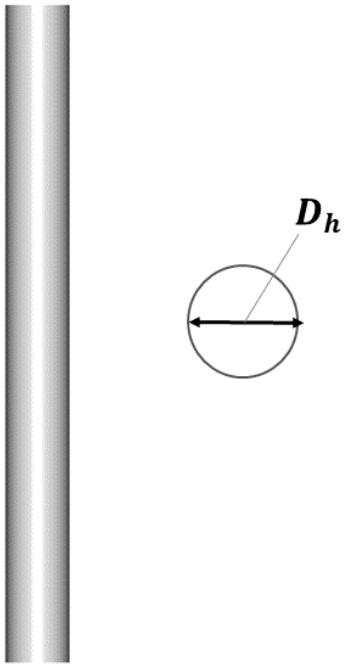

Figure 2.1: View Cylinder

D [mm]	L [mm]
22	220

Table 2.1: Geometrical Parameters of the Cylinder

2.2 Vibrissa-shaped Cylinder

A vibrissa-shaped cylinder (SVC) is used to compare our results with those already obtained in the literature and with the CC. Its geometrical parameters (Table 2.2) are chosen to align with previous studies [30, 5] maintaining a total volume similar to that of the CC. The SVC geometry was designed using *Inventor*® 3D CAD software by *AutoDesk*. As shown in Figure 2.3, the SVC is composed of an

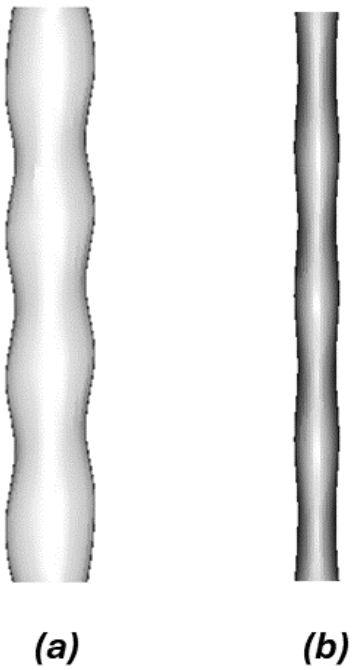

Figure 2.2: (a) Frontal View Vibrissa, (b) Side View Vibrissa

λ [mm]	l [mm]	k [mm]	a [mm]	b [mm]	α [°]	β [°]
27.5	8.6	14.3	7.3	17.8	15.3	17.6

Table 2.2: Geometrical Parameters of the Vibrissa

elliptical cross-section that changes periodically along the span, where λ represents the value of half the wavelength. The wavelength is defined as the distance between the two centre point of the two ellipses, the maximum one and minimum one which are respectively the nodal and the saddle cross-sections. The changing elliptical cross-section along the span gives the vibrissa its typical wavy edges. At the top points along the two edges, the nodal cross-section is associated, defined by an ellipse with a semi-minor axis

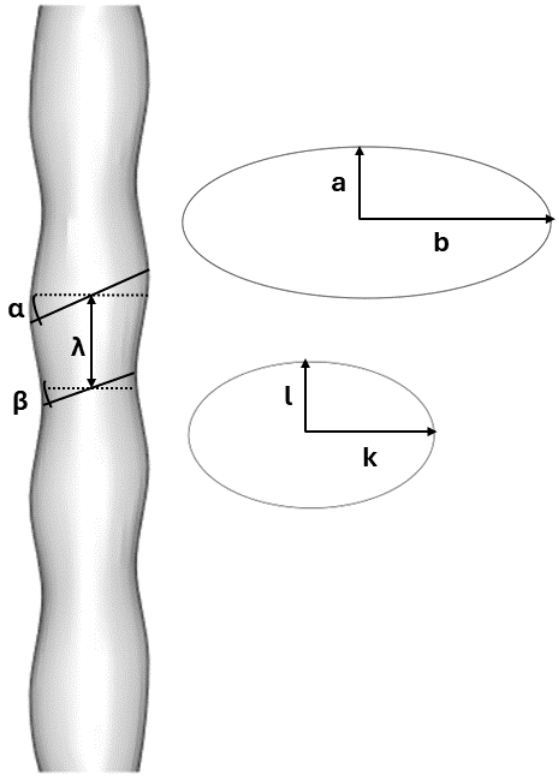

Figure 2.3: The upper ellipse denotes a nodal plane and the lower ellipse denotes a saddle plane

value of a and a semi-major axis value of b. For the bottom points, the saddle cross-section is associated, with parameters l as the semi-minor axis and k as the semi-major axis. The distance between the centres of these two ellipses is λ. Another important feature is that the two wavy edges are not aligned. They are shifted due to the inclination, in the plane of the cross-section, given to the elliptical saddle and nodal cross-sections. For the saddle one, the value is β, while for the nodal one, the value is α. In summary, the SVC is a cylinder with wavy edges and inclined elliptical cross-sections. Thus, the SVC is defined by seven geometrical parameters that give it special geometrical features reflecting different fluid dynamic behaviour.

Chapter 3

Computational method

3.0.1 Flow Solver

The commercial software **3DS Simulia PowerFLOW** version 6 has been used. It is based on the *Lattice Boltzmann Method* (LBM). The discretized version of the continuous Boltzmann equation, both in space and time, is solved [14]:

$$\frac{\partial g}{\partial t} + \vec{\xi}\frac{\partial g}{\partial \vec{x}} + \vec{F}\frac{\partial g}{\partial \vec{\xi}} = \Omega \tag{3.1}$$

The distribution function $g(\vec{\xi}, \vec{x}, t)$ defines the probability for an existing particle at point $[\vec{x}, \vec{x} + \Delta\vec{x}]$ within the time step $[t, t+\Delta t]$ with velocity $[\vec{\xi}, \vec{\xi}+\Delta\vec{\xi}]$. The left side of the equation represents the particles' transport and the influence of external forces, such as gravity, on their behavior. On the right-hand side, the BGK-Collision-Operator [26] describes the interaction between particles:

$$\Omega = -\frac{1}{\tau}(g - g^{eq}); \tag{3.2}$$

where τ is the relaxation time and g^{eq} is the equilibrium distribution function derived from the Maxwellian-Boltzmann equilibrium distribution.
The distribution of particles is solved by means of the LB equation on a Cartesian mesh, named the lattice; the discrete volume elements are called voxels. Particles can move along discrete directions with discrete velocities at discrete time intervals. Following the standard DkQb model notation [36], where k stands for the dimension of space and b represents the number of discrete velocity directions, a D3Q19 lattice scheme has been employed.
A Very Large Eddy Simulation (VLES) approach has been employed to resolve only the larger turbulence scales. The sub-grid scales are accounted for by adding a turbulent relaxation time to the viscous relaxation time using a turbulence model, based on the two equation Renormalization Group Theory (RNG) $k-\varepsilon$ [36]:

$$\tau_{\text{eff}} = \tau + C_\mu \frac{\frac{k^2}{\varepsilon}}{(1+\eta^2)^{1/2}}, \tag{3.3}$$

where $C_\mu = 0.09$ and η are a combination of the local strain, local vorticity, and local helicity parameters. The term η allows for mitigation of the sub-grid scale viscosity, in the presence of large resolved vortical structures.
The solver uses an extended turbulent wall model that dynamically incorporates the presence of a pressure

gradient (PGE-WM) [32]. This model takes into account the effect of the pressure gradient by rescaling the length-scale y^+, in the generalised law-of-the-wall [19], by a scaling parameter A:

$$u^+ = \frac{1}{\kappa}\ln(\frac{y^+}{A}) + B; \tag{3.4}$$

where $B = 5.0$, $\kappa = 0.41$, $y^+ = \frac{(u_\tau y)}{\nu}$, and A is a function of the pressure gradient. Parameter A captures the physical consequence of the velocity profile slowing down and expanding due to the pressure gradient. The parameter A is defined as proposed by *Texeira et al.* [32]:

$$A = \begin{cases} 1 + \frac{\beta\left|\frac{dp}{ds}\right|}{\tau_w} & ,\mathbf{u_s}\cdot\frac{dp}{ds} > 0 \\ 1 & \text{otherwise} \end{cases} \tag{3.5}$$

where τ_w is the wall shear stress, $\frac{dp}{ds}$ is the streamwise pressure gradient, and β is a length of the same order of the unresolved near-wall region.

Chapter 4

Simulations

4.1 Settings

To achieve results that accurately reproduce fluid dynamic phenomena, the methodology has involved evaluating different computational grids to conduct a convergence analysis. This analysis determined the appropriate level of refinement for the studied problem. The convergence analysis began with a coarse computational grid to initialise the solution, followed by refinement to an higher level grid, allowing for the assessment of convergence trends for specific parameters relevant to the problem.
Mesh generation was performed using the *PowerCASE* interface within the *PowerFLOW* software. This interface allows for the creation or importation of geometries, definition of domains and computational boxes, specification of boundary conditions, and simulation parameters. Additionally, it automates these tasks through equation definition. It is worth noting that this work focused on defining parameters related to free flow, where the fluid is air, taken from the study by *Smith*, *Chen*, and *Zang* [30]:

V_∞ $[\frac{m}{s}]$	D_{ref} $[mm]$	Re_∞	T_∞ $[K]$
25	22	37000	288.5

Table 4.1: Parameters of the Cylinder and Free-Stream Conditions

The dynamic viscosity is evaluated from temperature using the Sutherland equation:

$$\mu = \mu_{ref} \left(\frac{T}{T_{ref}} \right)^{\frac{3}{2}} \frac{T_{ref} + S}{T + S}, \tag{4.1}$$

where μ_{ref} is the viscosity at reference temperature (T_{ref}), and S is the Sutherland constant. Using the dynamic viscosity from the Reynolds number definition, the density is evaluated:

$$\rho = \frac{Re\mu}{VD}, \tag{4.2}$$

and subsequently, the pressure from the ideal gas law:

$$p = \rho \frac{R}{M} T, \tag{4.3}$$

where R is the universal gas constant and M is the molar mass of air. Among the free flow parameters, we also calculate the Mach number to confirm the low Mach number condition (M«1):

$$M = \frac{V}{\sqrt{\gamma \frac{R}{M} T}}, \tag{4.4}$$

where γ is the heat capacity ratio. Once the free-stream parameters have been defined, the simulation

$\rho_\infty \ [\frac{kg}{m^3}]$	$p_\infty \ [Pa]$	M_∞
1.205	99780.4	0.0734

Table 4.2: Free-Stream Parameters

volume must be specified. The dimensions of the simulation volume are $60 \times D_{ref}$ upstream and downstream in the x direction, and $40 \times D_{ref}$ above and below in the y direction. The geometry has a span of $10 \times D_{ref}$ and is bounded at either end in the z-direction, where a periodic boundary condition is applied. Within this volume, 12 additional boxes of various sizes are defined. These 13 boxes allow us to define the Variable Resolution (VR) levels, each associated with a different cell size. It is important to note that the mesh definition is automatically performed by *PowerFLOW*, which defines a structured grid with cubic voxels. Furthermore, at each VR level, the cell size is doubled compared to the previous level. All boxes are shown in Figure 4.1. In addition to the various boxes of different VR levels, there are two cylindrical areas defined as sponges. These sponges are high viscosity regions designed to dampen the reflection of acoustic waves. Finally, it is important to note that there is a red box present in the domain. This area represents the boundary enclosing the noise sources. As seen in Figure 4.1, the inlet, outlet, top, and bottom zones are defined at the edges of the simulation volume, to which the boundary conditions are assigned. It is important to note that the flow direction is in the positive x direction. The defined conditions include outlet conditions for the top, bottom, and outlet zones, where the free-stream flow direction and static pressure of the free-stream are specified. For the inlet zone, the inlet condition is applied, setting both pressure and velocity to match the free-stream reference values. The upstream velocity, given the geometry in cross-flow, is defined perpendicular to the geometry axis, thus in the streamwise direction along the x-axis. Additionally, the turbulence intensity of the upstream flow is set to ensure a low turbulence level ($I = 0.001$). Finally, a standard wall condition is defined on the surface of the geometry. The simulation and saving parameters are then defined. It is essential for the correct evaluation of the results to assess a proper and fully developed flow field. Therefore, considering a flow pass time, which is the time required for the upstream velocity flow to pass over the diameter, of $10 \times D_{ref}/V_\infty$. Based on this, a total simulation time of 25 times the flow pass time is defined, with a conservative transient period of 15 times the flow pass time. Consequently, the remaining time will be the simulated and sampled period where the flow will be properly developed. Finally, a sampling frequency of $9090.91Hz$ was evaluated; this value was chosen by taking 4 times the maximum frequency that was intended to be resolved within the acoustic spectrum. The value of 4 was chosen conservatively from the application of the Nyquist theorem, while the maximum frequency was evaluated as 10 times the shedding

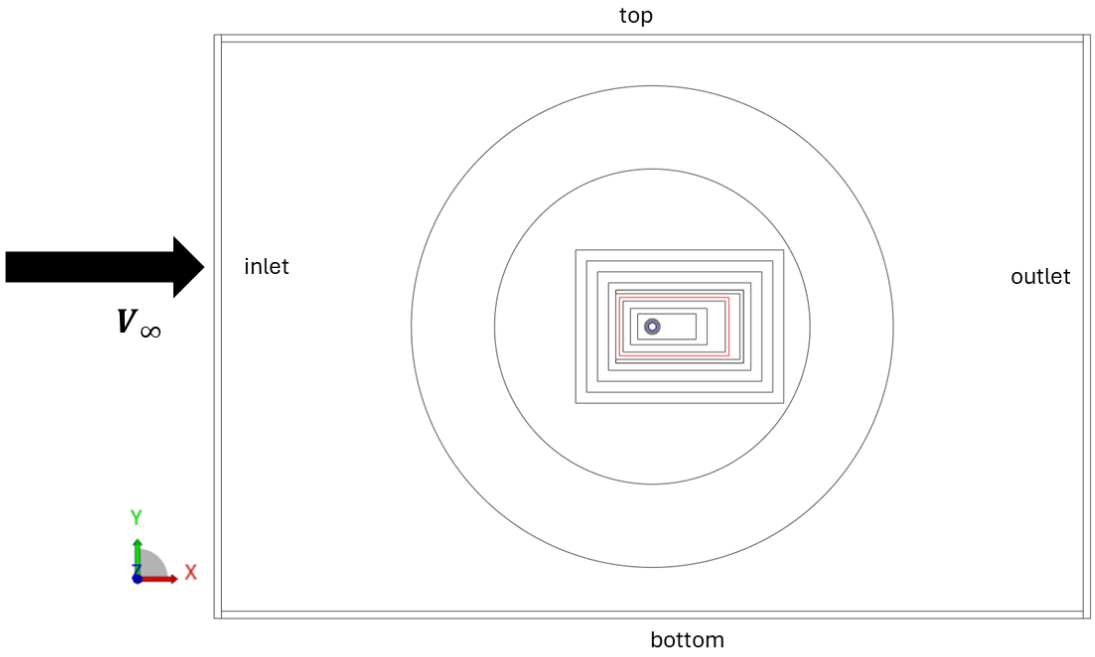

Figure 4.1: Simulation Volume

frequency of the phenomenon under examination. The choice of this maximum frequency falls within the range of the acoustic spectrum proposed in the literature [30] and is therefore suitable for comparison. Furthermore, the shedding frequency was evaluated using the Strouhal number formula, considering the expected value of this number, in relation to the diagram shown in the Figure 1.5 in the Chapter , of 0.2:

$$f_s = \frac{StV_\infty}{D_{ref}} = 227.2727Hz; \tag{4.5}$$

The last important sampling parameter is the minimum resolved frequency, which is evaluated as the inverse of the flow pass time times the saving time. Its value is: $11.36Hz$.

Flow Pass Time $[sec]$	*Transient Time* $[sec]$	*Simulation Time* $[sec]$	*Sampling Frequency* $[Hz]$
$10 \times \frac{D_{ref}}{V_\infty} = 10 \times 8.8 \times 10^{-4}$	0.132	0.22	9090.91

Table 4.3: Simulation Parameters

The convergence study involved meshes of different refinement levels. With each mesh change, the resolution was increased. The resolution is defined as the number of cells along the diameter, thus the smallest cell size, which is associated with the higher VR level, can be calculated from this. Furthermore, given the value of the wall cell size, it is possible to evaluate the value of y^+. y^+ is a dimensionless parameter that measures the distance from the first grid cell to the surface and determines the accuracy of the boundary layer thickness prediction.

$$y^+ = \frac{u_\tau y}{\mu}, \tag{4.6}$$

where u_τ is the friction velocity, y is the wall distance, and μ is the kinematic viscosity of the fluid. In CFD, the y^+ value is crucial for determining the accuracy of the boundary layer thickness.

4.2 Circular Cylinder

4.2.1 Mesh convergence

The first simulated geometry was that of the cylinder geometry (CC) described in Chapter 2. At first, three different meshes were evaluated:

Coarse Mesh	*Intermediate Mesh*	*Refined Mesh*
$resolution = 51.2$	$resolution = 102.4$	$resolution = 204.8$
$\Delta x = 0.000429687$ m	$\Delta x = 0.000214844$ m	$\Delta x = 0.000107422$ m
$y^+ = 40$	$y^+ = 20$	$y^+ = 10$

Table 4.4: Meshes' Definitions for Circular Cylinder

The first simulation involved a brief calculation with a coarse refinement mesh solely for the purpose of initialising the first true simulation with the coarse mesh. This simulation involved a mesh of approximately 6.3×10^5 cubic voxels for a total of $241,568$ timesteps. Additionally, given the total sampling time, the number of evaluated shedding cycles is 20. Indeed, considering the saving time (0.088 sec) and the shedding frequency in Equation 4.1, the number of shedding cycles within this time interval is that. It should be noted that this value is preserved in every simulation across different meshes. Given the coarse nature of the mesh, the expected results were anticipated to be incorrect in terms of capturing the real physical phenomenon. This was confirmed both by the evaluation of the pressure coefficient, focusing on the separation point, and by the acoustic spectrum, focusing on the peak acoustic frequency. However, what was important to validate in this simulation was the shape of the spectrum, ensuring it resembled the acoustic spectrum of a circular cylinder in cross-flow. Once this spectrum was validated, the solution was used to initialise the subsequent simulation with an intermediate resolution mesh. The purpose of a doubled resolution mesh is to evaluate the trend of certain characteristic parameters under examination, such as the separation point and the shedding frequency. The intermediate resolution mesh involved 2.7×10^6 cubic voxels for a total of $603,920$ timesteps. The evaluation of the results showed that the parameters of interest for the study of convergence exhibited a positive trend. Therefore, a further simulation was performed on a more refined mesh, which led to the near convergence of the results. By convergence of results, it is meant that they become independent of the mesh resolution and thus, a further level of refinement does not lead to significant variations in terms of improvement of them. This simulation involved 4.7×10^7 cubic voxels and $1,207,841$ timesteps. The comparison in terms of the convergence of the separation point, shown in Figure 4.3, and the peak frequency in the acoustic spectrum, shown in Figure 4.5, indicated the need for an additional simulation with doubled refinement to achieve complete grid convergence. Therefore, a new simulation was performed with a final mesh defined in Table 4.5. This final simulation involved 3.9×10^8 cubic voxels, where the distribution is shown in Figure 4.2, and 2,415,682 timesteps, with a seconds-to-timestep ratio of: 0.3965 sec. Looking at the Figure 4.3, it is evident how the trend of the pressure coefficient changes from coarser to finer meshes. The improvement occurs mainly in terms of capturing the correct separation point, which in the subcritical regime as it ($Re = 37000$) is around 90° as discussed in Chapter 4.1. The point is perfectly captured in the simulation with a resolution corresponding to a y^+ value of 5, and the change in the behaviour of the up and down

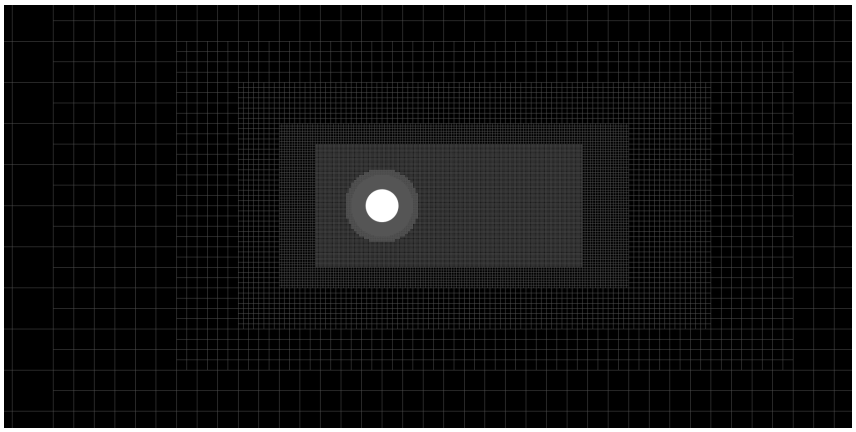

(a) cross-sectional grid

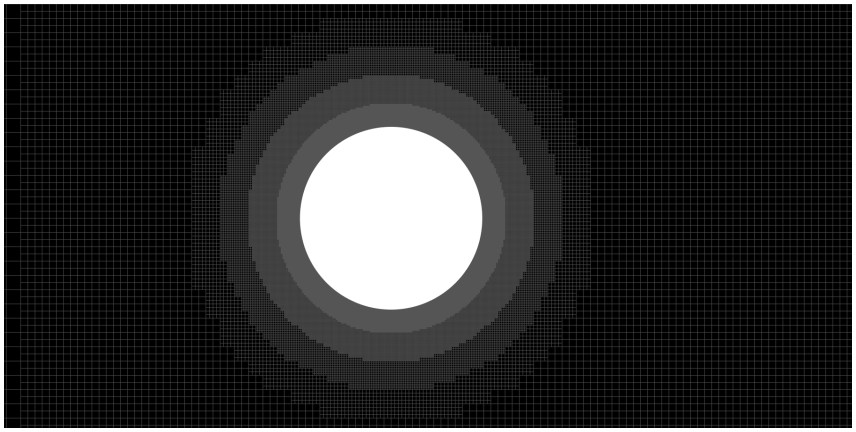

(b) cross-sectional grid zoom

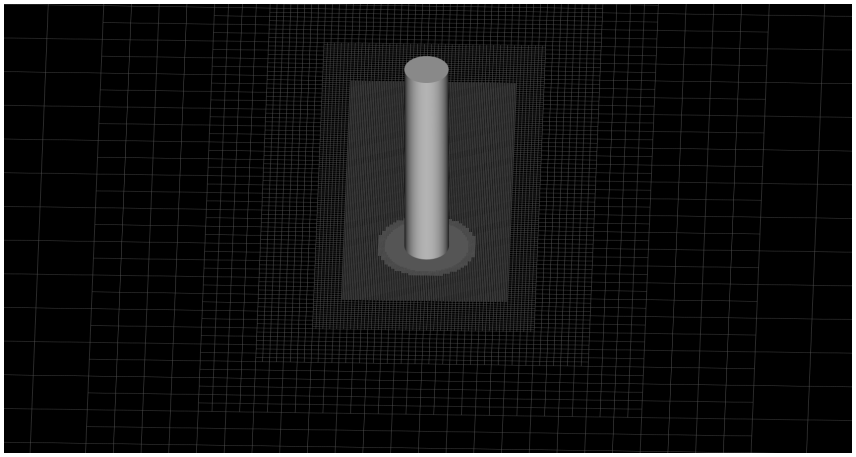

(c) grid distributions around the cylinder

Figure 4.2: CC Mesh

Most refined Mesh
$resolution = 409.6$
$\Delta x = 5.37109$ e-05 m
$y^+ = 5$

Table 4.5: Final Refined Meshes' Definitions for Circular Cylinder

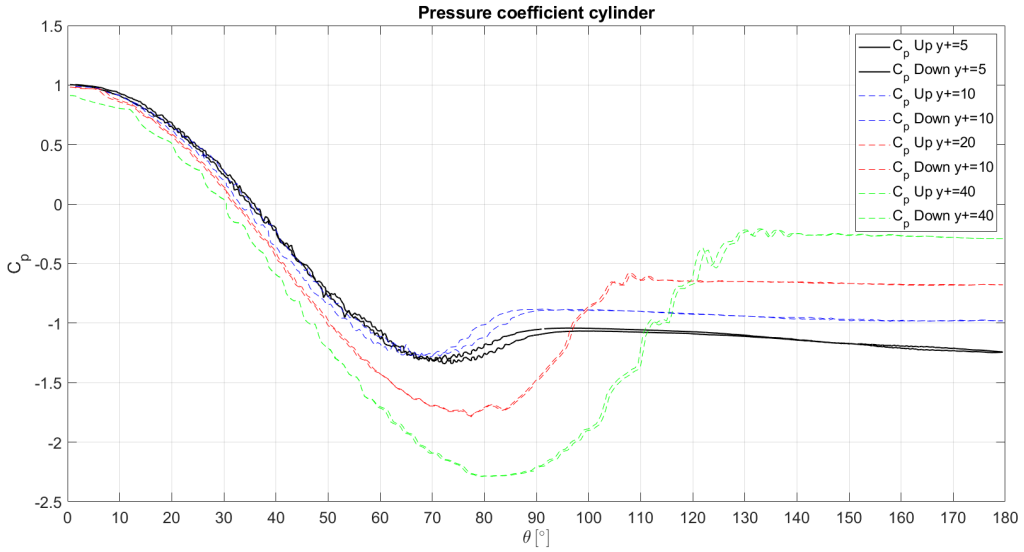

Figure 4.3: Pressure coefficient for the four different meshes

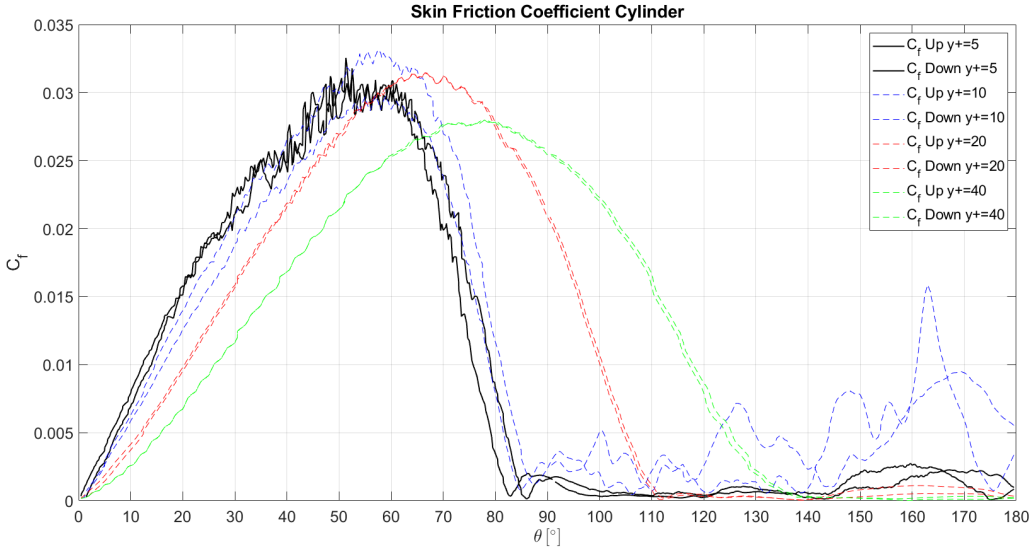

Figure 4.4: Skin friction coefficient for the four different meshes

curves between the last two higher resolution meshes appears minimal; in fact, up to the separation point, these curves overlap almost entirely.

The findings regarding the separation point in the pressure coefficient graph are supported by the

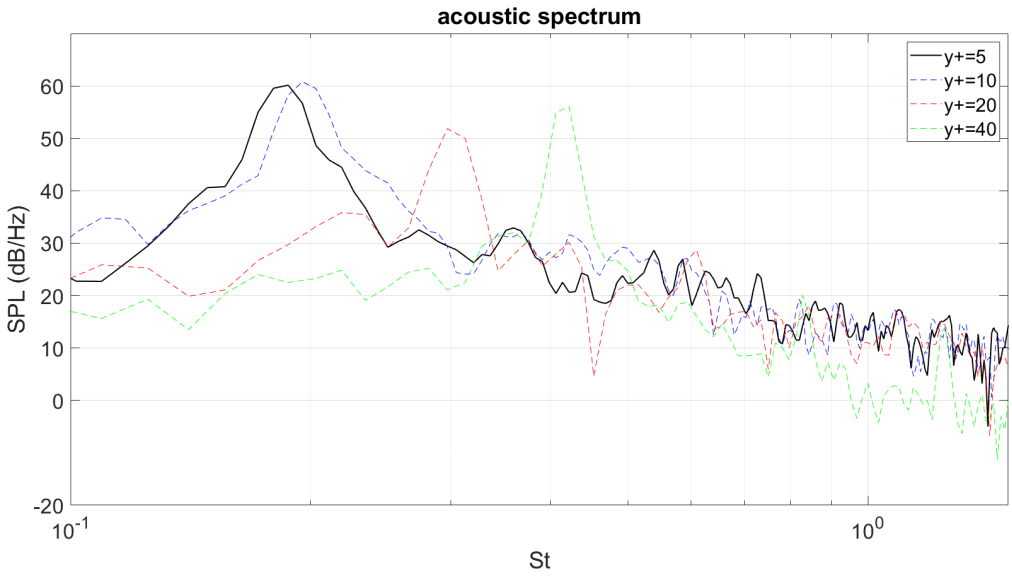

Figure 4.5: Aeroacoustic spectrum for the four different meshes

comparison with the friction coefficient, in Figure 4.4. In this case as well, the trends tend to improve with grid resolution, accurately capturing the exact separation point. What appears unusual is the presence of slight peaks beyond the separation point in the curves for a grid resolution with $y^+ = 10$, suggesting a unusual reattachment downstream of the cylinder in the separation zone. However, this phenomenon completely disappears in the simulation with the subsequent grid resolution.
Regarding the acoustic spectrum at different resolutions, it is observed that it takes on the typical characteristic shape of a bluff body like a circular cylinder, with a peak frequency around that of shedding and a subsequent decrease in SPL values at higher frequencies, as discussed in Chapter 4.1. It is important to highlight that the acoustic spectrum was evaluated in the far-field using the *PowerACOUSTICS* software, which enables to predict the amount of far-field noise using acoustic analogy method that solves the Ffowcs Williams–Hawkings (FW-H) equation. The far-field evaluation point was chosen in accordance with that of the reference [30] paper to validate its results. The point is located 1.75 meters above the midspan. The assessment of noise level is conducted in terms of Sound Pressure Level (SPL), which is expressed by the equation:

$$SPL = 10 \log_{10}(\frac{p_{xx}}{P_{\text{ref}}^2}) \tag{4.7}$$

where p_{xx} represents the Power Spectral Density (PSD) of the acoustic pressure. Here, P_{ref} denotes the reference pressure, with $P_{\text{ref}} = 20\ \mu Pa$. From this comparison, it can be interpreted that the two lower-resolution grids fail to capture the underlying physics due to the presence of peaks at higher frequencies. This is likely due to the fluid dynamic cause of noise originating from vortex shedding which needs to be captured by grids with appropriately sized cells due to the presence of regions with strong gradients. It is likely that the two grids with the lowest resolution are composed of cells that are too large, averaging over too large a space and failing to capture the real physical phenomenon at play. Transitioning to the two grids with increased resolution, the difference between them is almost negligible at high frequencies, while there is a shift of the acoustic peak towards slightly lower frequencies. However, it is noteworthy that for the grid with a resolution corresponding to a $y^+ = 5$ value, there is the presence of the second harmonic peak, which is located at twice the frequency of the first peak, and the disappearance at high frequencies of two peaks whose origin is not well understood and they could be related to that unusual reattachment

showed in the skin friction plot. Therefore, based on the results presented, the grid convergence study was considered concluded, and the results obtained from the simulation with a grid resolution corresponding to $y^+ = 5$ were evaluated.

4.2.2 Validation

Once grid convergence was achieved, validation of the results was conducted against those obtained in the reference paper by *Smith*, *Chen*, and *Zang* in "*Aeroacoustic performance of a seal vibrissa shaped cylinder*" [30]. It should be noted that the simulations were performed under conditions of fluid dynamic similarity at a Reynolds number of 37000 and using the same geometry in terms of diameter and span length.
The first comparison was made in terms of the Strouhal number, mean drag coefficient, and the root-mean-square (RMS) of the lift fluctuations, as shown in Table 4.6. From the comparison of the Strouhal

Reference data			
Re	St	$\bar{C_D}$	$C_l^{'}$
3.7x10^4	0.19	1.28	0.40
Simulated data			
Re	St	$\bar{C_D}$	$C_l^{'}$
3.7x10^4	0.19	1.18	0.41

Table 4.6: Comparison of CC data

number, mean drag and fluctuating lift coefficients, a close agreement between the simulated results and the reference data can be observed. This comparison was then extended to the entire acoustic spectrum as depicted in the Figure 4.6. The spectrum was limited to a range of Strouhal values between 0.1 and 1.5 for

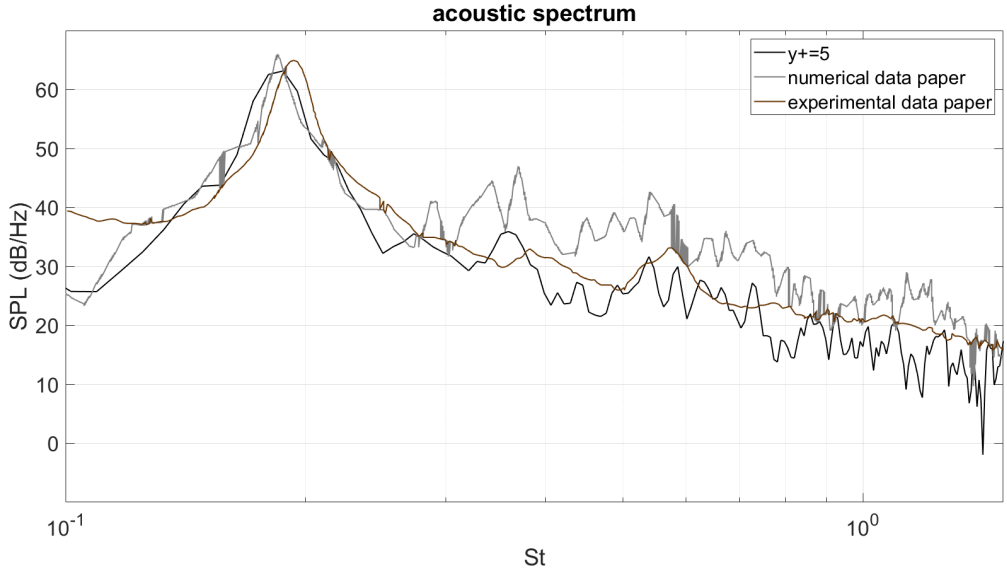

Figure 4.6: Comparison of the aeroacoustic spectrum for CC

better comparison with the range presented in the spectra proposed by the reference paper. The results presented in the paper are from both numerical CFD analysis and experimental testing. The trend of the acoustic spectrum obtained closely matches the experimental reference at high frequencies, while there is a shift towards lower frequencies of the primary aeolian tone. This shift is also observed for the second

harmonic, which, however, exhibits a higher SPL value in our results. The primary tone aligns closely with and overlaps the one obtained from the literature's numerical analysis, although no higher harmonics are captured in the literature's results, and the noise level at higher frequencies is higher compared to what we obtained. An additional validation of the obtained results concerns the comparison of the average

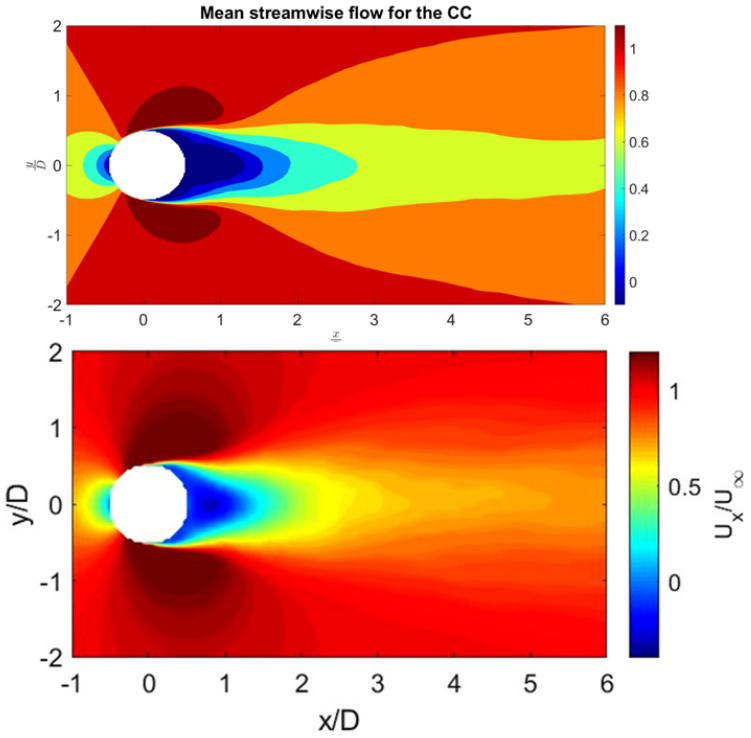

Figure 4.7: Comparison of time-averaged streamwise flow for CC

streamwise flow for the CC, in the contour plot the streamwise velocity is non-dimensionalised with the free-stream velocity. The map in the Figure 4.7 shows the dimensionless streamwise velocity with respect to the free-stream velocity. The image presents the map obtained from our simulation in the upper part, while the lower part represents that from the reference paper. The area of interest for comparison is the recirculation zone downstream of the cylinder, which exhibits a streamwise extent of approximately 1.3D and is comparable to that shown in the paper. Moreover, the longitudinal extension itself is comparable. Based on the results presented, the simulation was considered validated, and we proceeded to simulate the SVC.

4.3 Vibrissa-Shaped Cylinder

4.3.1 Mesh convergence

Once convergence of the grid on the cylinder was achieved, the validity and convergence of the grid on the vibrissa were evaluated. The simulation parameters are the same as those defined for the CC and shown in the Table 4.3, along with the definition of the 3 grids and the 3 resolution levels shown in the table 4.4. The geometry of the Vibrissa-Shaped Cylinder (SVC) was accurately defined in Chapter 2.2 and is used as the geometry for the second phase of evaluating its aeroacoustic properties. The simulation volume is the same as that used for the Circular Cylinder case and shown in the Figure 4.1. For the vibrissa,

the grid convergence evaluation process followed the same steps as for the CC, as already explained in the dedicated Section 4.2. The grid convergence was assessed by analysing the trends of the pressure coefficient and the acoustic spectrum, which are shown respectively in the Figure 4.10 and in the Figure 4.12. As already presented in Chapter 1.2.3, in the horizontal direction, the results for the vibrissa are shown for the nodal (Figure 4.9) and saddle planes (Figure 4.8).

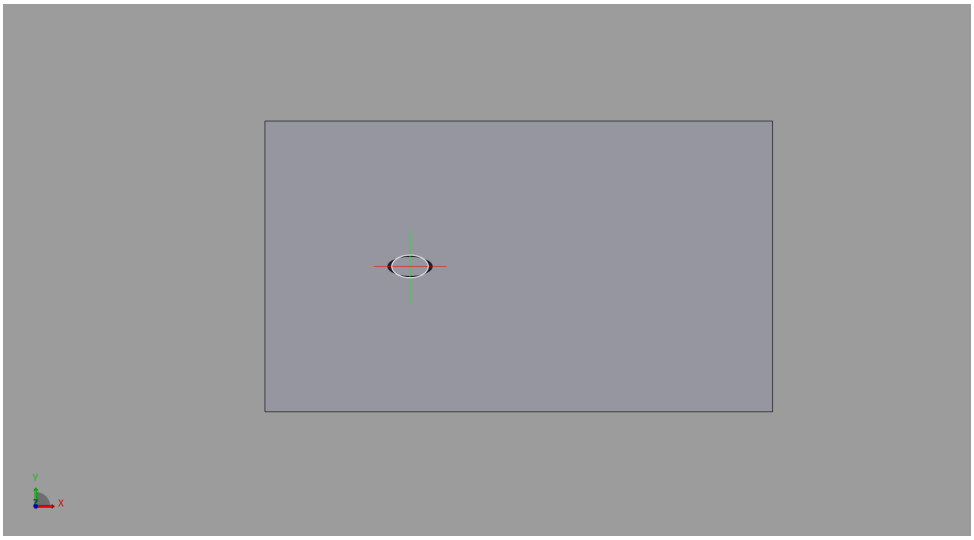

(a) x-y cut

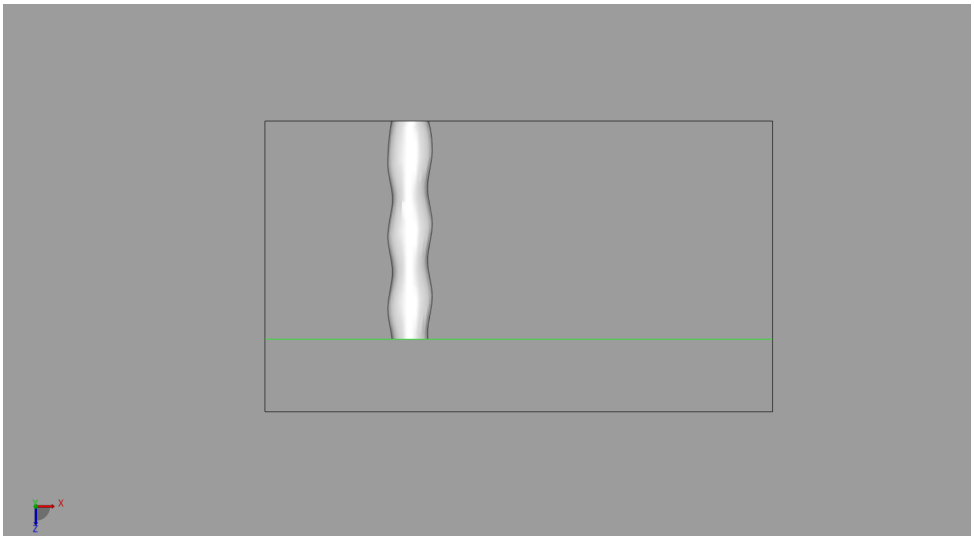

(b) x-z cut

Figure 4.8: Saddle plane

As shown in Figures 4.10, 4.11 and 4.12, the grid convergence is satisfactory although not complete. The pressure coefficient graphs (Figure 4.10) in the nodal and saddle planes demonstrate a significant improvement in grid resolution, i.e., at a value of $y^+ = 10$. One can observe an almost completely overlapping of up and down curves which relates to the symmetry of the section. This property is upheld by the highest-resolution grid. Additionally, there is a better capture of the separation point, which is located at approximately 0.005 m for the nodal plane and approximately -0.002 m for the saddle plane.

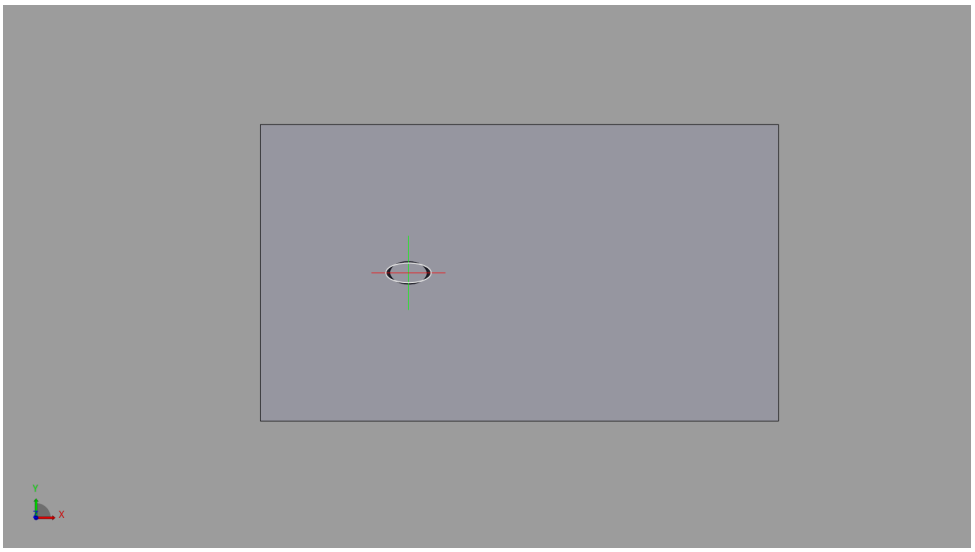

(a) x-y cut

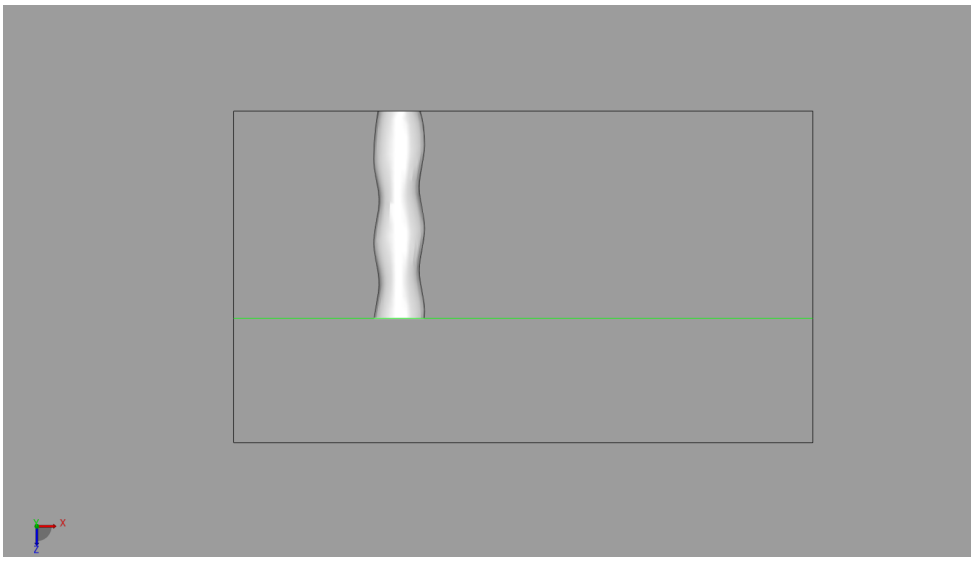

(b) x-z cut

Figure 4.9: Nodal plane

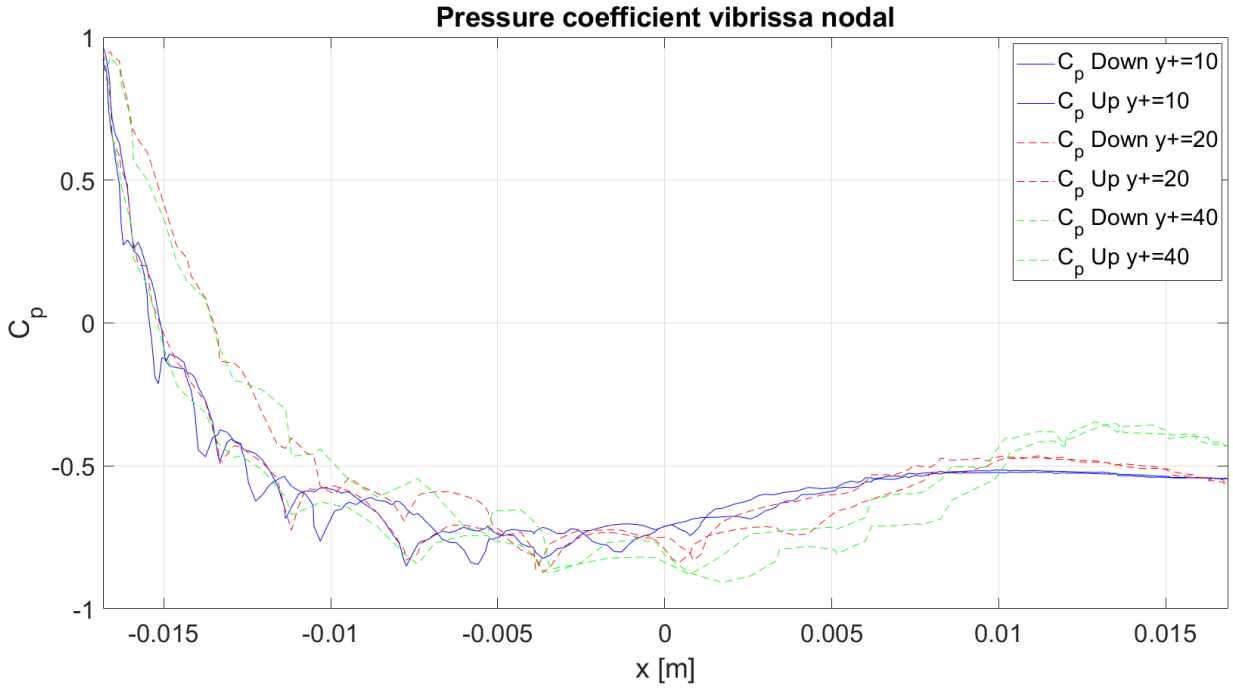

(a) Nodal Plane

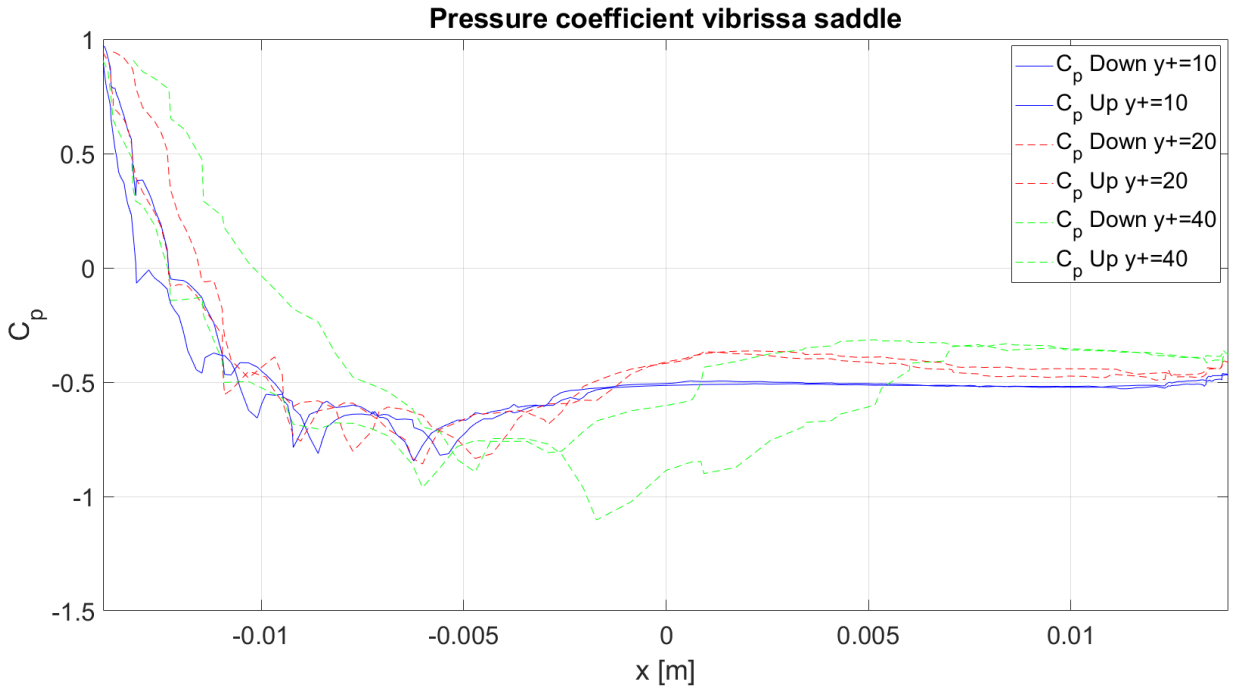

(b) Saddle Plane

Figure 4.10: Pressure Coefficient for the three different meshes

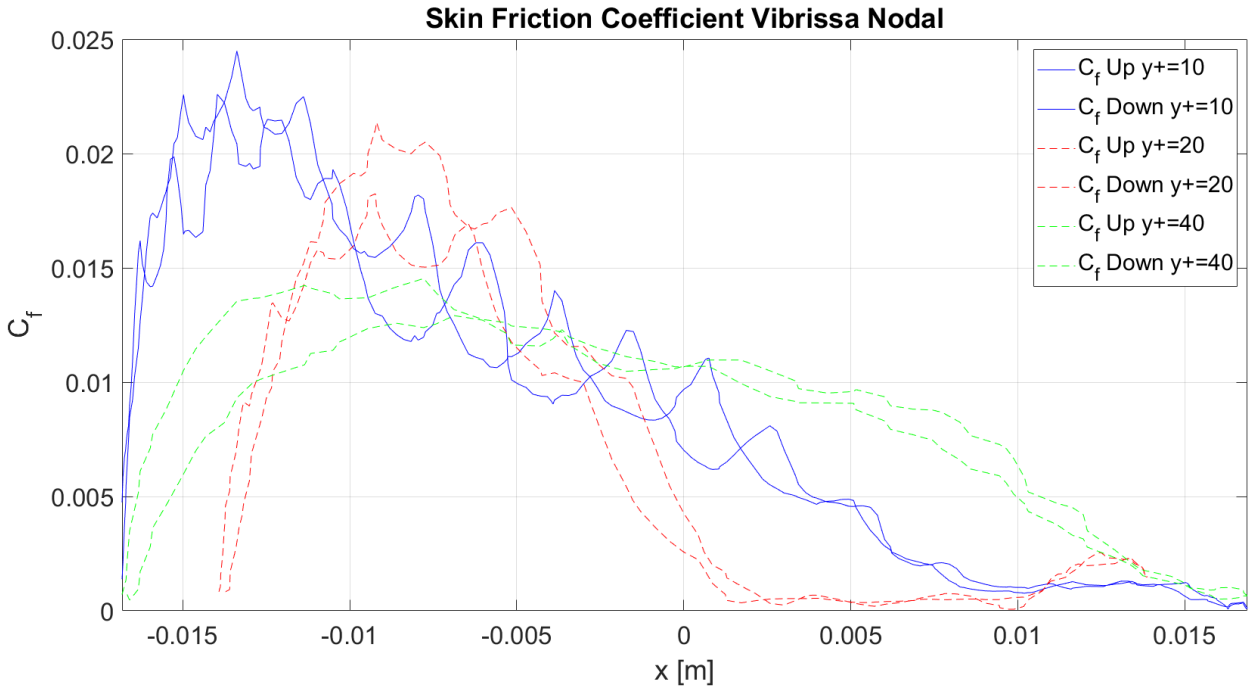

(a) Nodal Plane

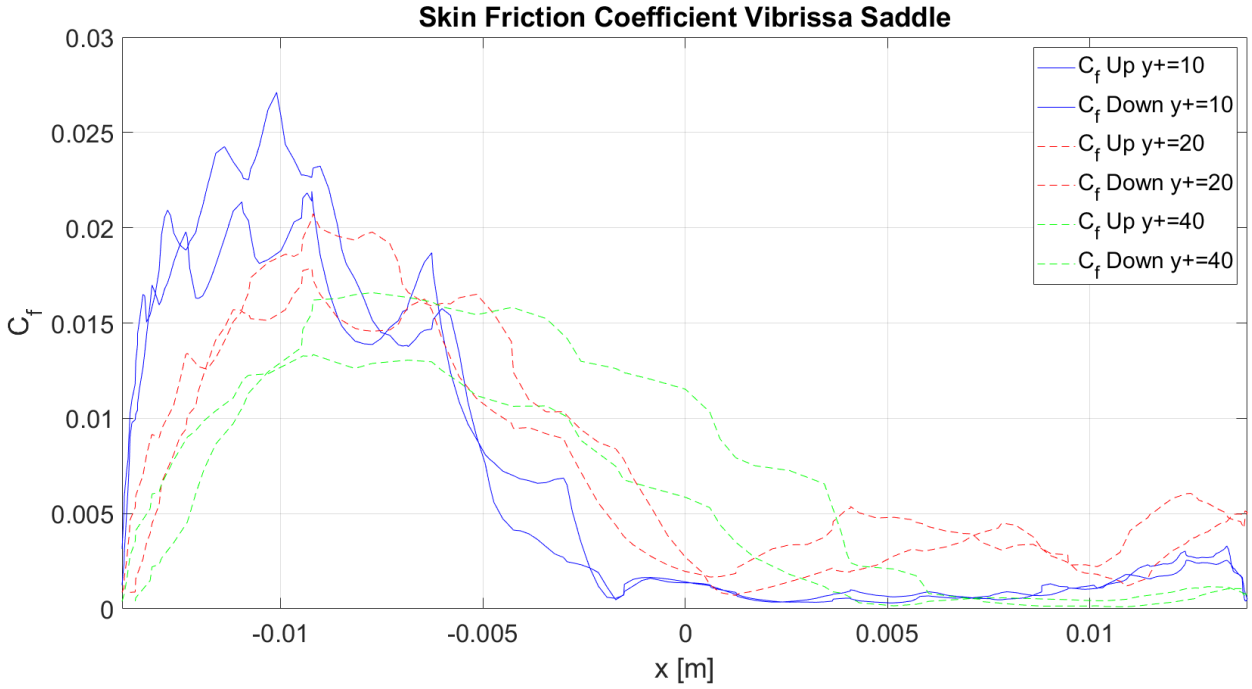

(b) Saddle Plane

Figure 4.11: Skin friction Coefficient for the three different meshes

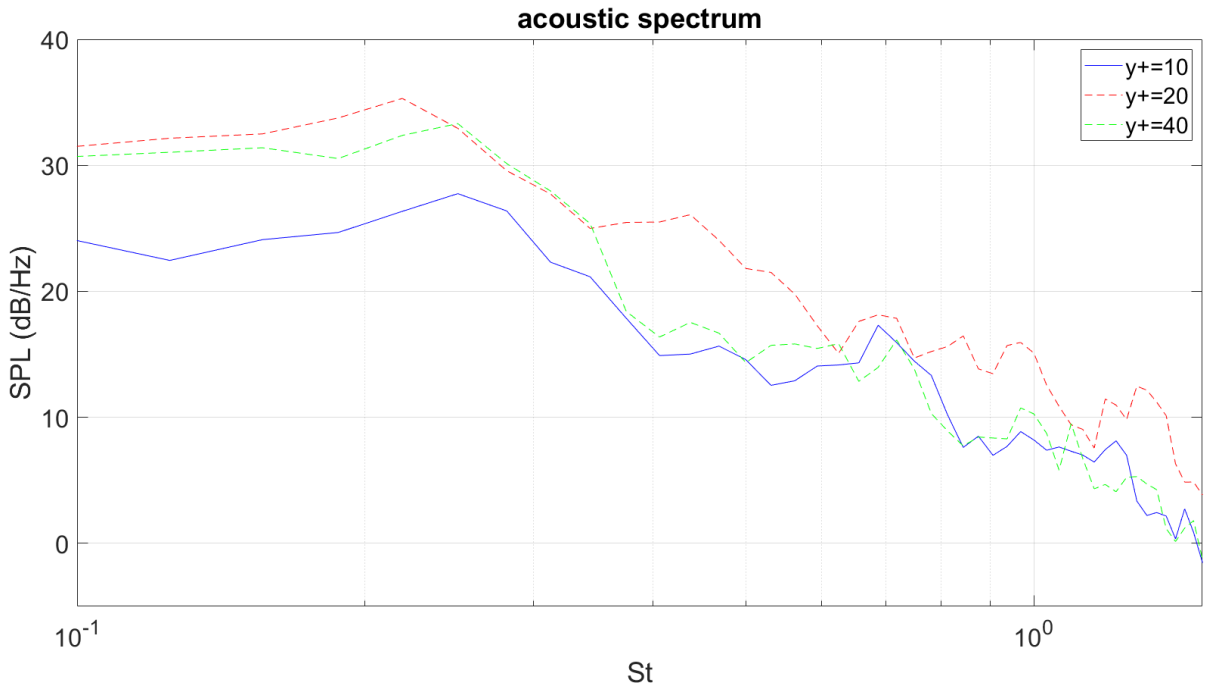

Figure 4.12: Aeroacoustic Spectrum for the three different meshes

This difference aligns with the distinct geometric characteristics of the two sections.
In the saddle plane, the separation occurs in a position similar to that of a CC, due to the smaller major axis and larger minor axis relative to the nodal plane, making the ellipse more like a circular section. This is also confirmed in the study by *Wang* and *Liu* [34], where a comparison between a circular cylinder, an elliptical cylinder, and a vibrissa-shaped cylinder is shown. In the presentation of the time-averaged streamwise velocity in the horizontal plane, different longitudinal extents of recirculation zones can be observed. This is directly related to the point of separation; this point is located further downstream for an elliptical cylinder than for a circular one, thus also valid for the nodal plane, but the point of separation of the circular cylinder is closer to that of the saddle plane of the vibrissa. All this interpretation is linked to the aspect ratio (a/b) between the major and minor axes of the ellipse. A ratio of one represents a circle, and for the nodal plane, this ratio is 2.44, while for the saddle plane, it is 1.66.
Moreover, a reduced difference between the pressure coefficient trends for the $y^+ = 20$ and $y^+ = 10$ resolutions is also noted, indicating a tendency toward grid convergence. For perfect convergence, further simulation at double resolution, i.e., $y^+ = 5$ (as performed for the cylinder), is recommended. The decision to evaluate the results for the vibrissa at $y^+ = 10$ represents a compromise between simulation time and obtained results. The results presented here are sufficiently accurate to show the different aeroacoustic performance and explain their fluid dynamic causes, considering that an estimated time to complete the double-resolution simulation at $y^+ = 5$ for the SVC was about 200 days, considering a seconds-to-timestep ratio of 8.642 sec and a total number of timesteps of 2,415,682. In this case as well, the trend of the skin friction coefficients aligns with those of the pressure coefficient. The imperfect alignment that seems to exist between the up and down curves is actually illusory, as the curves follow the same trend but are shifted. This is likely due to how the files are exported from the graphical visualisation software *PowerVIZ*.
It is emphasised, however, that regions beyond the separation where a slight reattachment is observed are also present in this case, especially for the grid with $y^+ = 20$ and in the saddle plane. Given the more pronounced presence for the curves on the saddle plane and that this characteristic has also been observed

in the cylinder, one might think that it is related to a difficulty in accurately capturing the recirculation zone of the sections with greater separation.
Similar conclusions about grid convergence can be drawn by evaluating the acoustic spectrum in Figure 4.12 which is evaluated at the same point in the far field of the CC case. Despite a noticeable difference at lower frequencies, it can be observed that at higher frequencies, the trend is almost independent of the grid resolution. In conclusion, based on the results presented and the computation times, validation of the obtained results was conducted on the final, refined mesh with $y^+ = 10$. This mesh consists of approximately 1.4x10^8 cubic voxels. Figure 4.15, 4.13, 4.14 show the visualisation of this mesh, which is structured using the same boxes as those used for the CC, but with offsets adapted to the elliptical shape of the SVC section.

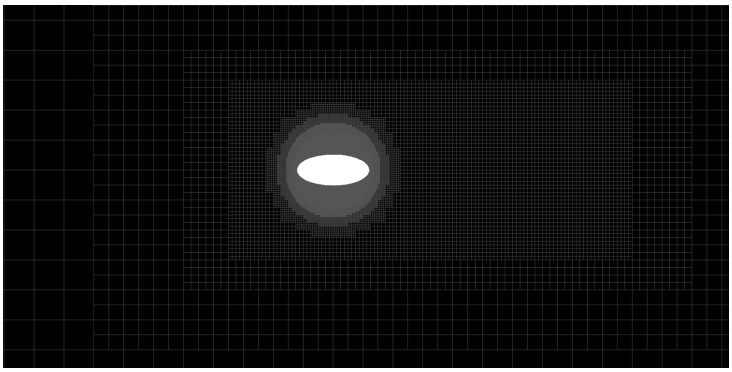

(a) cross-sectional grid

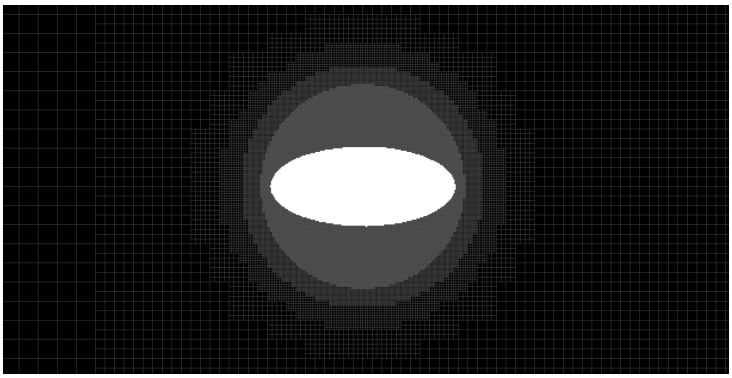

(b) cross-sectional grid zoom

Figure 4.13: Mesh SVC nodal plane

4.3.2 Validation

The second part of the analysis focused on validating the obtained results in relation to those proposed in the reference paper [30]. Even for SVC the first comparison was made in terms of mean drag coefficient, and the root-mean-square (rms) of the lift fluctuations, as shown in Table 4.7, where the values have been non-dimensionalised using the same parameters as used for the CC, i.e. as the reference area the cylinder diameter times the span length. The Strouhal number is not present in the validation due to the different acoustic spectrum generated by the SVC. The simulated SVC demonstrates a good agreement in terms of mean drag coefficient and root-mean-square of lift fluctuations, which are notably lower compared to those shown for the cylinder in the Table 4.6. This difference will be analysed in the following Section

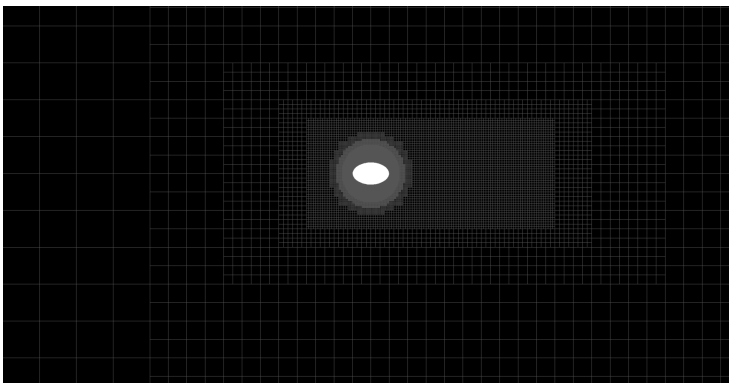

(a) cross-sectional grid

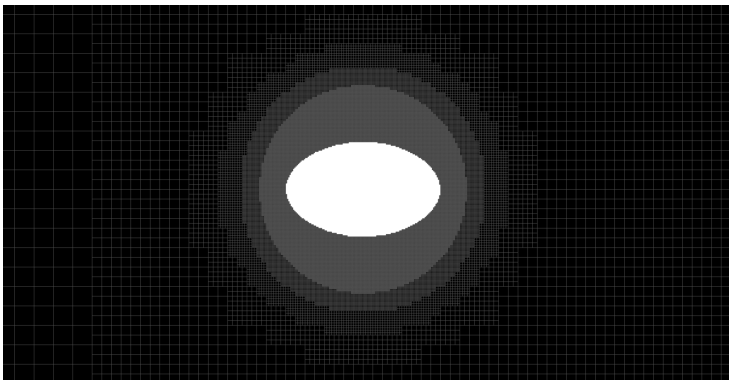

(b) cross-sectional grid zoom

Figure 4.14: Mesh SVC saddle plane

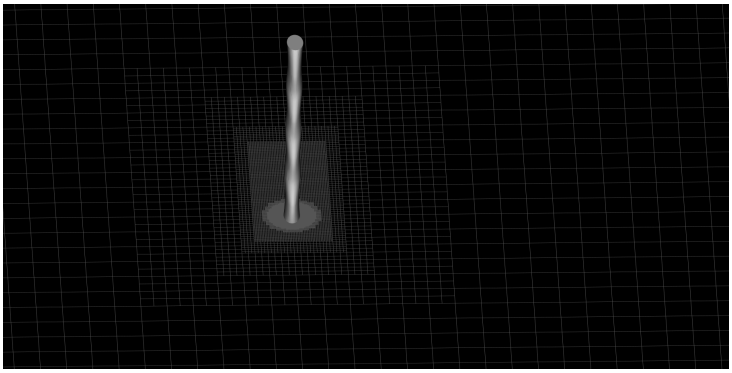

Figure 4.15: Grid distributions around the cylinder

Reference data		
Re	$\bar{C_D}$	$C_l^{'}$
3.7x10^4	0.44	0.020
Simulated data		
Re	$\bar{C_D}$	$C_l^{'}$
3.7x10^4	0.40	0.035

Table 4.7: Comparison of SVC data

4.4. Continuing with the validation, the entire acoustic spectrum was then compared, in Figure 4.16. The comparison of noise levels for the SVC between the obtained data and those from the paper shows a good similarity. Although the obtained values are lower than the experimental ones reported in the paper, they exhibit greater conformity with the numerically simulated reference results. It is important to note that, due to the proximity between the experimental noise level and the wind tunnel noise level, the experimental reference data were not used to validate their numerical data. However, it can be observed that the acoustic spectrum obtained displays the same broadband hump in the St range between 0.2 and 0.3 presents in the experimental reference data but that it is not captured in their numerical data. At low frequencies, there is an intermediate noise level between the simulated reference and the experimental results, while at high frequencies, the trend aligns with the simulated reference level. In addition, it was deemed appropriate to compare the time-averaged streamwise flow to validate the fluid dynamic results, where the streamwise velocity is non-dimensionalised with the free-stream velocity. The comparison was conducted for both the nodal and saddle planes, as shown in Figure 4.17 in (a) and (b), respectively. As observed, the saddle plane exhibits a larger recirculation zone due to its larger upwind area compared to that of the nodal plane, Indeed, it stretches out with the decrease in the aspect ratio (a/b). What is notably consistent is the extension of the recirculation zone, indicated by the darker blue region, extending approximately 2D downstream of the section. In contrast, for the nodal plane, this area is significantly reduced in longitudinal and streamwise directions, extending only around 1.5D downstream of the section but with an higher value of the ratio $\frac{u_x}{U_\infty}$ and thus, more stable. Furthermore, both results show that the recirculation zone of the saddle section suffers a greater loss of velocity than that of the nodal plane. The nodal plane also has a faster recovery of free-stream velocity beyond the recirculation zone. Therefore, in light of the comparison showing good agreement in the rms of the fluctuating lift coefficient and the mean drag coefficient, as well as the acoustic spectrum and fluid dynamic results, the simulation is considered validated. The next step involves comparing them with the CC results.

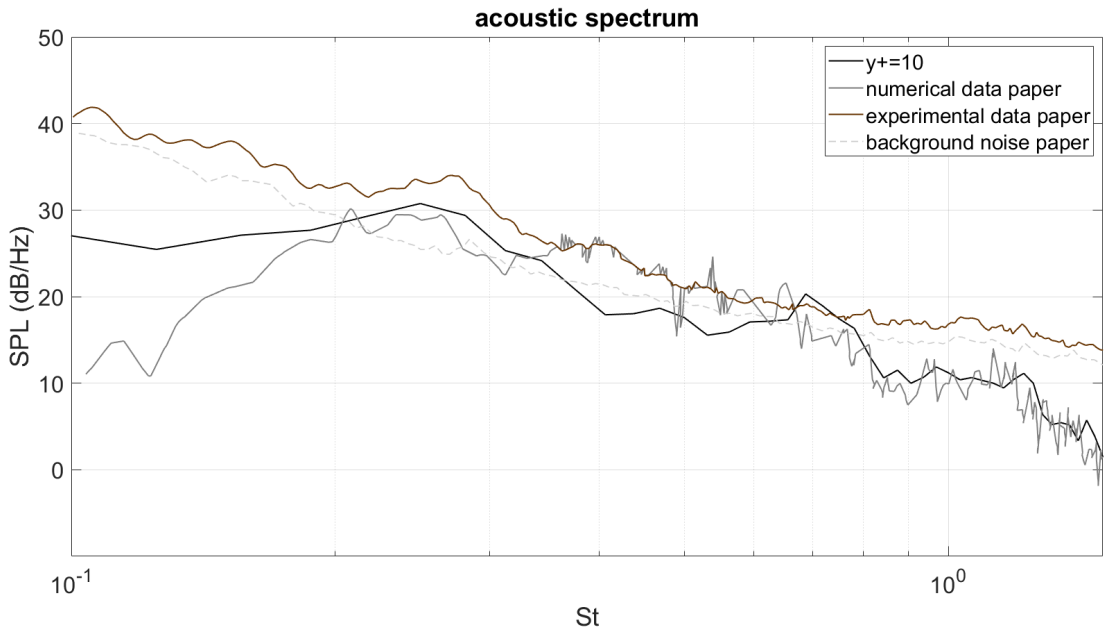

Figure 4.16: Comparison of the aeroacoustic spectrum for SVC

4.4 Results

The final part of the analysis focused on comparing the results obtained for the CC and SVC to evaluate the acoustic performance of the SVC in terms of its noise reduction capability and to investigate the fluid dynamic causes of this different behaviour. The first significant result arises from the comparison of the acoustic spectra generated by the two geometries, as presented in Figure 4.18. It is evident how the SPL of the SVC is significantly lower across all frequencies.Analysing the two spectra, in the SVC one it is important to note the absence of the typical acoustic tone associated with regular fluctuations in lift due to vortex shedding, which is present in the CC one, at around a St of 0.19. This pattern could be linked to a different fluid dynamic phenomenon. However, there is a slight hump in the range of $0.2 \leq \mathrm{St} \leq 0.3$, which might suggest reduced, unsynchronized lift fluctuations at a not specific frequency value. Regarding the CC, the tonal peak is around $\mathrm{St} = 0.19$, and there is also noticeable presence of the second harmonic around $\mathrm{St} = 0.36$.

This leads us to present the comparison of drag and lift coefficients for the CC and SVC, respectively in Figure 4.23 and in Figure 4.22, where they are plotted against the reduced time (t'), defined as the time divided by the period of shedding. As can be seen, the lift fluctuations alternate perfectly, showing the typical vortex shedding behaviour. Furthermore, the magnitude is reduced by an order of magnitude for the SVC compared to the CC. The CC lift fluctuations are also more strongly regular, and these characteristics explain the difference in acoustic spectrum between the two geometries. The distinct temporal trends of the lift coefficient demonstrate that the fluid dynamic phenomenon downstream of the two geometries is fundamentally different. Furthermore, the same drag is shown to be reduced, which aligns with the recirculation zones downstream of the different geometries being smaller and fewer for the SVC compared to the CC, shown in Figure 4.26. The drag fluctuations for the CC also appear alternating and more periodic compared to those of the SVC, and these fluctuations are associated with the presence of the second harmonic in the acoustic spectrum. The confirmation of this assertion can be observed in Figure 4.19 and Figure 4.20, where the power spectral density of lift and drag coefficient fluctuations is plotted. In fact, in the spectra of the lift and drag coefficient fluctuations, a peak at St =

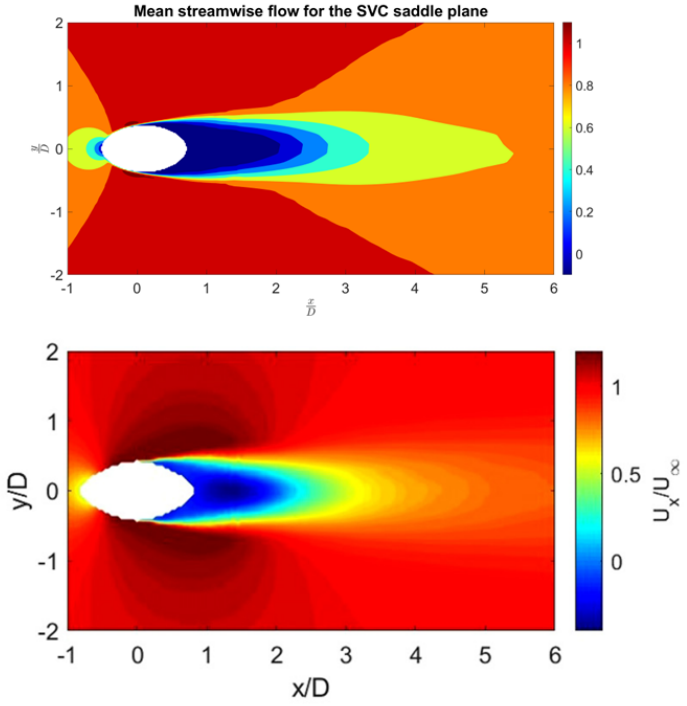

(a) saddle plane

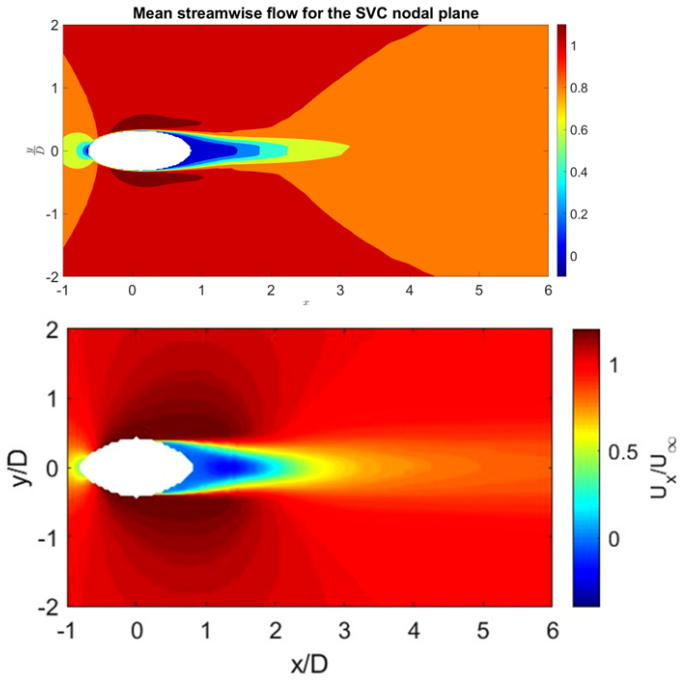

(b) nodal plane

Figure 4.17: Comparison of time-averaged streamwise flow for SVC

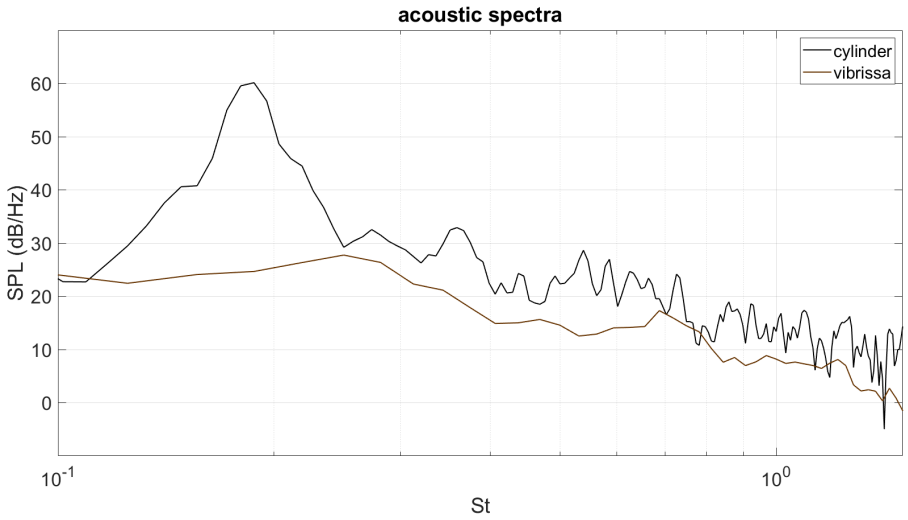

Figure 4.18: Acoustic spectrum for CC and SVC

0.195, that is close to the St=0.2 estimated in Section 4.1, is present for the lift and at St = 0.39 for the drag. Meanwhile, for the SVC, it can be observed that the spectrum shows energy spread across various frequency values, which is very noticeable in both graphs; this visualisation helps to explain the absence of synchronisation in the force fluctuations of already reduced magnitude. Moreover, to confirm that it has

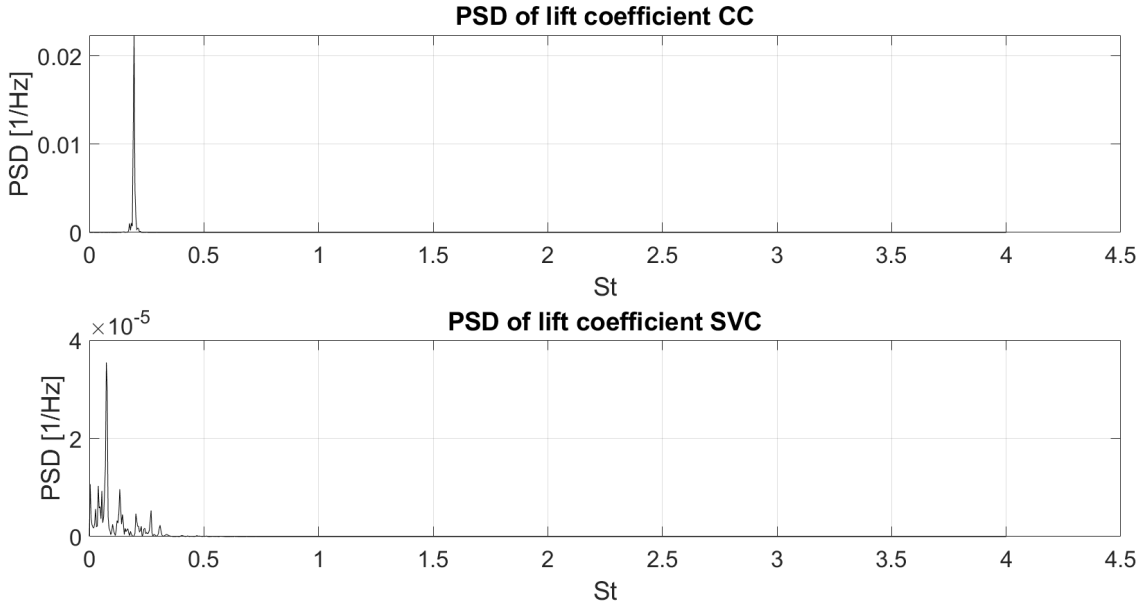

Figure 4.19: PSD of the lift coefficient fluctuations for CC and SVC

been plotted the acoustic spectrum at the same distance of 1.75 from the geometries but downstream the geometries respect to the midspan, shown in Figure 4.21. Now, for this spectrum, it is possible to observe the Aeolian tone associated with drag fluctuations at a value of approximately St = 0.38. This is due to the fact that the point is located in the direction in which the drag acts. What has been mentioned regarding a new pattern in the wake of the SVC, as opposed to the characteristic vortex shedding of the

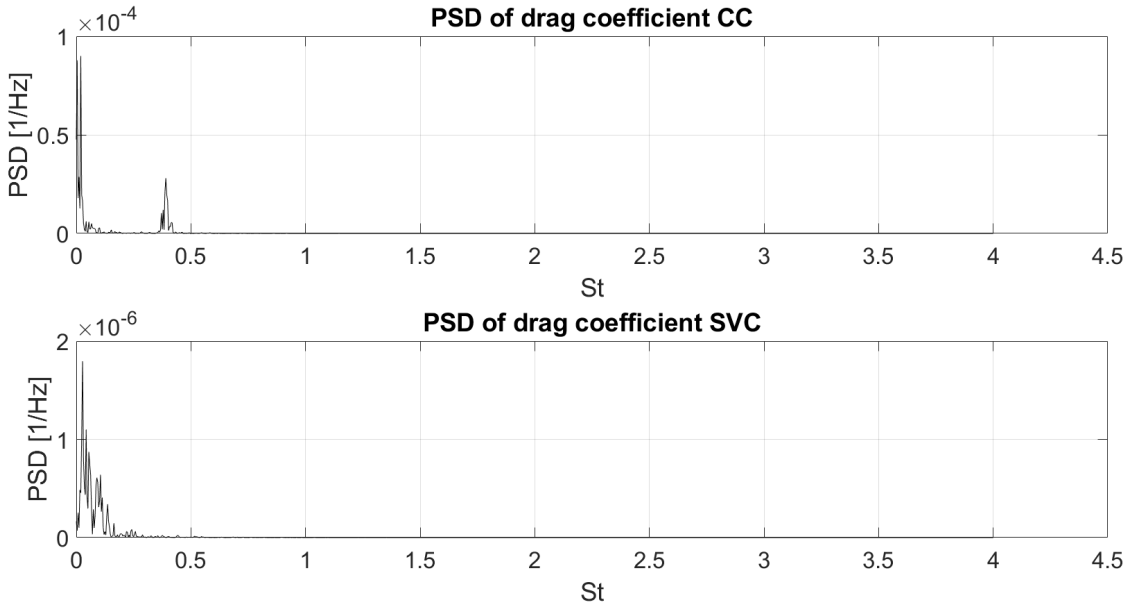

Figure 4.20: PSD of the drag coefficient fluctuations for CC and SVC

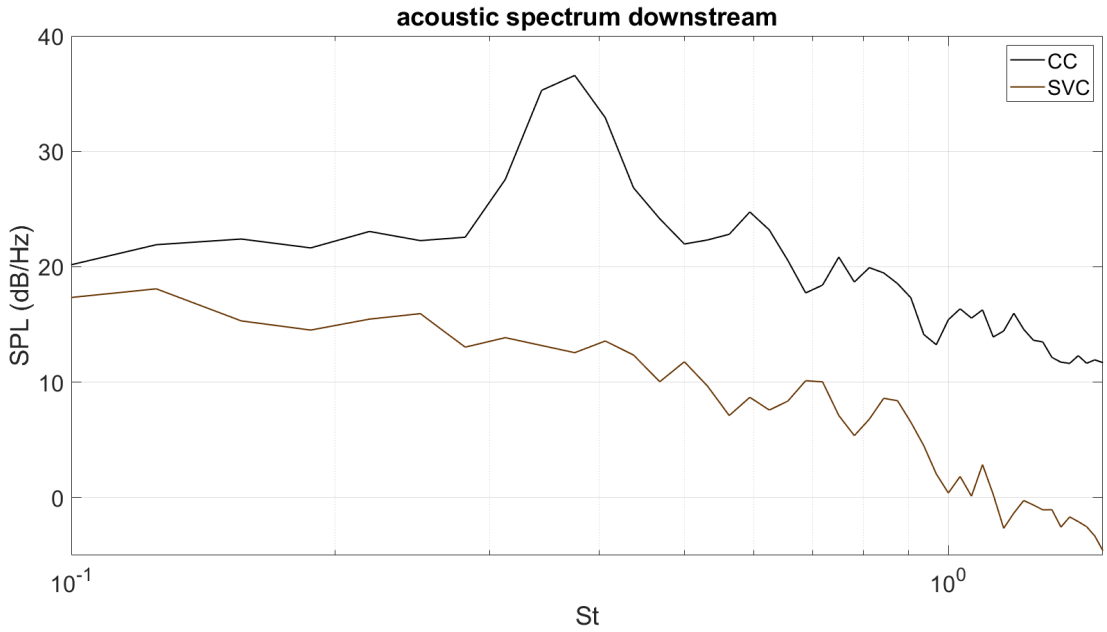

Figure 4.21: Acoustic spectra downstream CC and SVC

CC, can be clearly seen in the instantaneous time-averaged streamwise velocity field downstream of the geometries. In Figure 4.24, the instantaneous streamwise velocity field for the cylinder is shown at a moment characterised by a minimum and maximum value in the temporal fluctuation of C_l. The same is shown for the SVC in both the nodal and saddle planes in Figure 4.25. Basically, what is observed for the SVC is that, instead of the usual alternating vortices, the wake region has smaller, less coherent structures branching off from a more stable wake area.

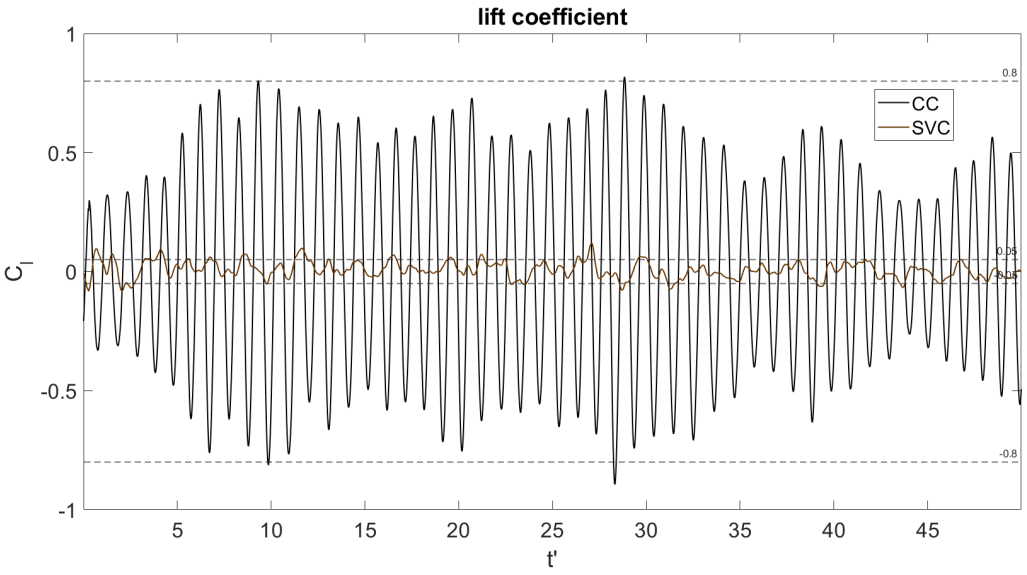

Figure 4.22: Lift coefficient for CC and SVC

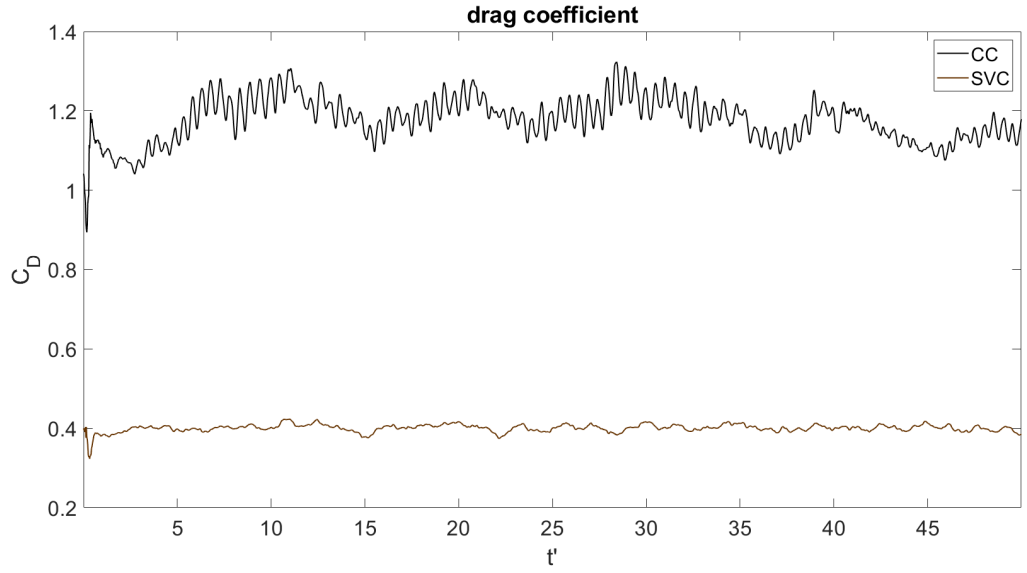

Figure 4.23: Drag coefficient for CC and SVC

At this point, it is interesting to understand the nature of the noise generated by the SVC and therefore analyse its directivity. In Figure 4.27, the directivity pattern for the overall SPL (OASPL) for both the CC and the SVC is shown. This polar diagram was created by defining several observers around a circumference, with the 90° point being the one used for evaluating acoustic spectra. Additionally, the upstream position corresponds to $\theta = 0°$ and the downstream position to $\theta = 180°$. The OASPL was obtained by integrating over a frequency range going from St of 0.1 and to 1.5. From the curve for the cylinder, it can be seen that its directivity is characteristic of a dipole source, confirming the nature of the noise due to lift fluctuations. Furthermore, the noise level at 90°, which is above the cylinder, is 74.8 dB. For the vibrissa, the noise level at 90° is 52.7 dB, showing a substantial reduction of about 22.1 dB in

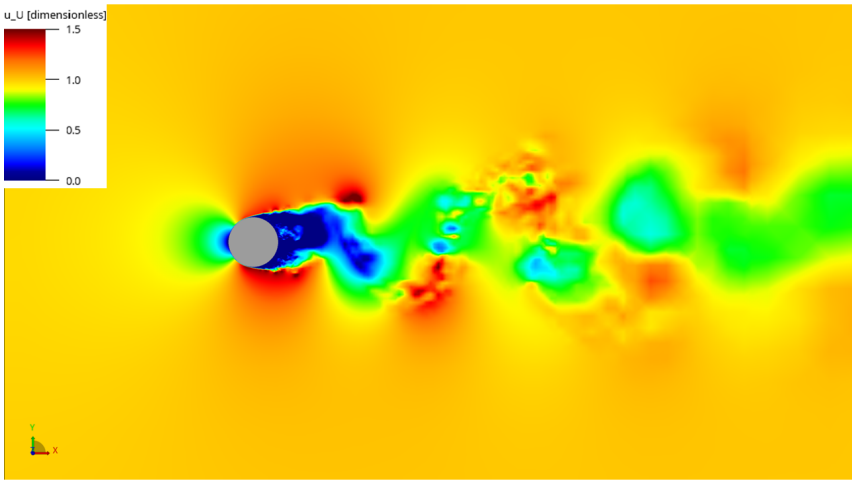

(a) low point in the lift cycle

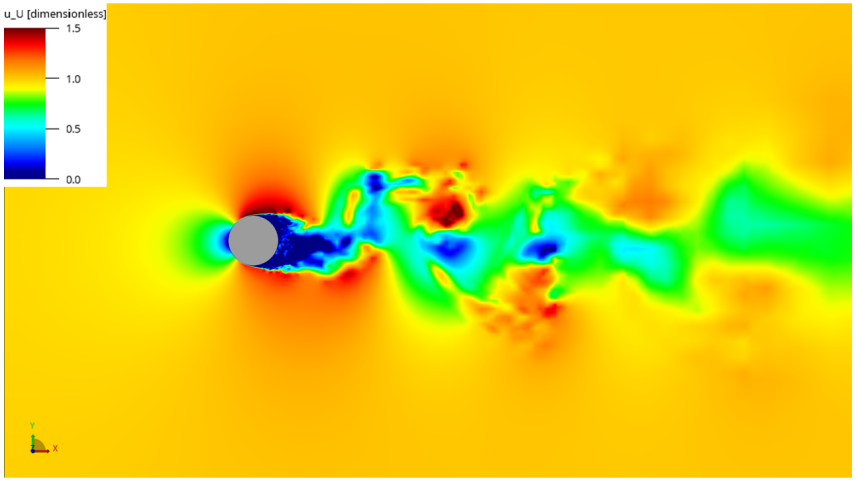

(b) up point in the lift cycle

Figure 4.24: Instantaneous streamwise velocity field at mid-span for CC

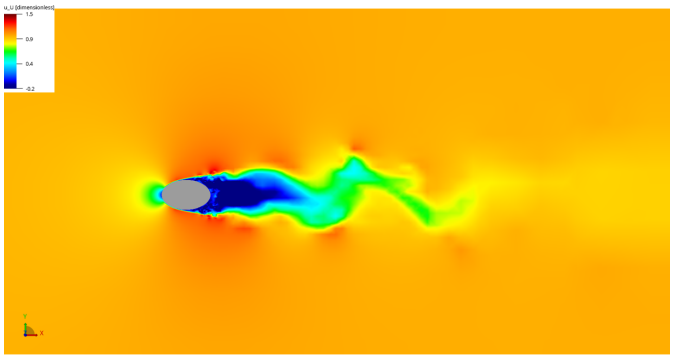

(a) low point in the lift cycle at saddle plane

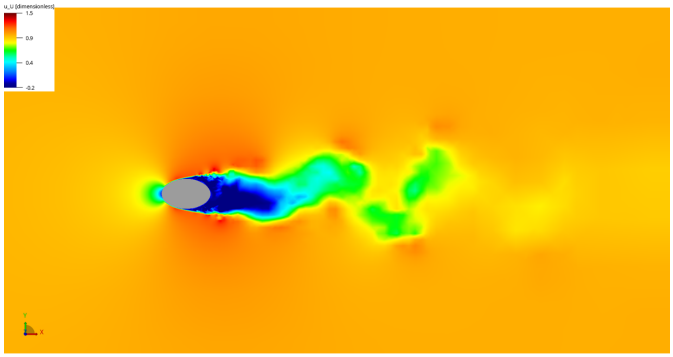

(b) up point in the lift cycle at saddle plane

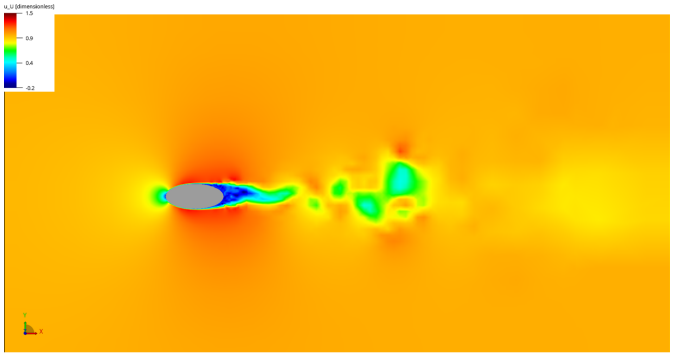

(c) low point in the lift cycle at nodal plane

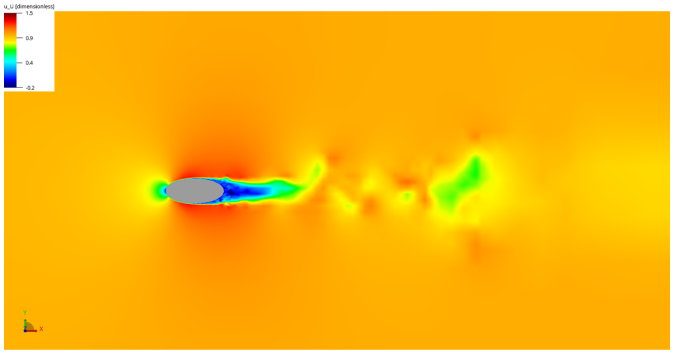

(d) up point in the lift cycle at nodal plane

Figure 4.25: Instantaneous streamwise velocity field for SVC

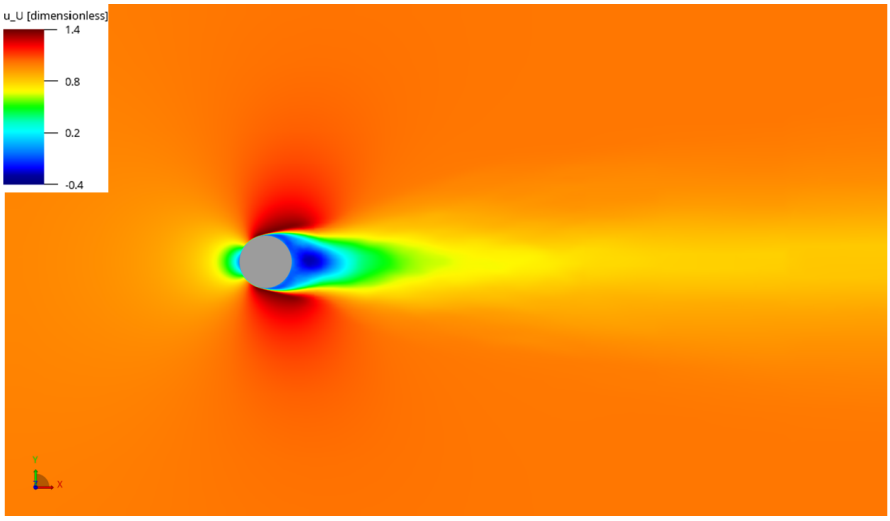

(a) CC

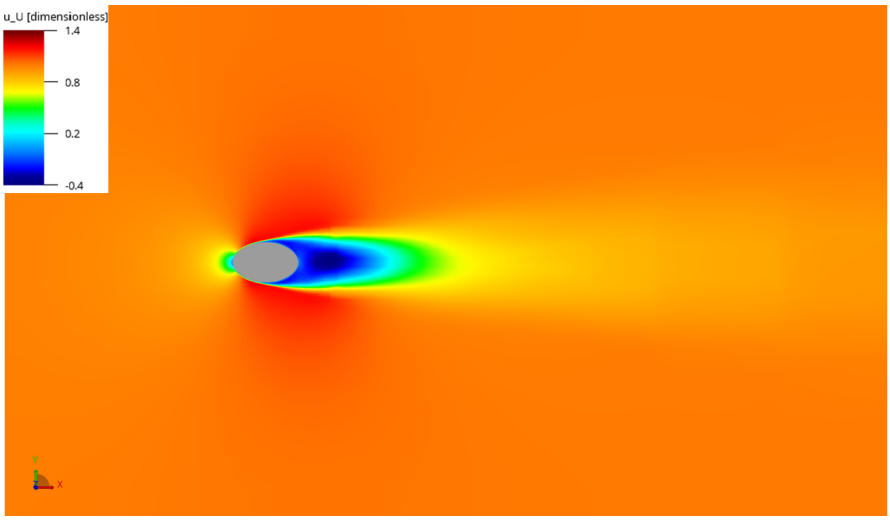

(b) SVC saddle plane

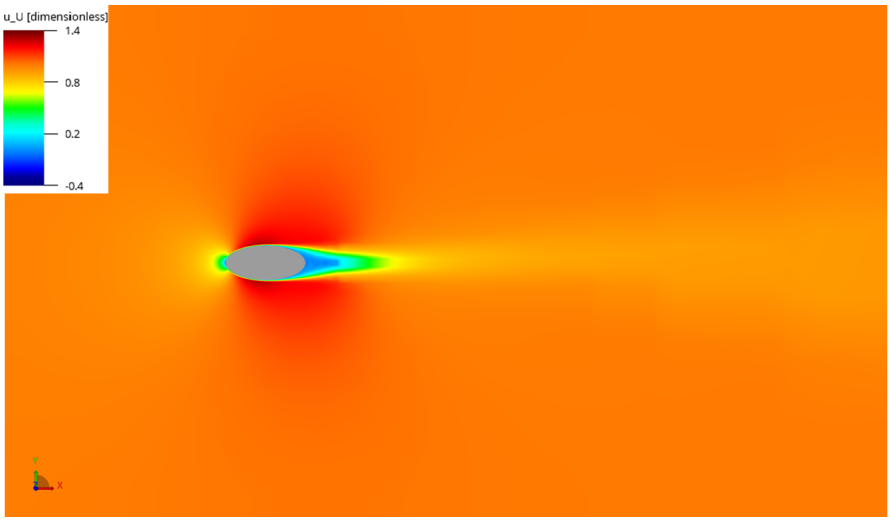

(c) SVC nodal plane

Figure 4.26: Time-averaged streamwise flow

total. This result is consistent with the one presented in the reference paper[30]. However, the directivity pattern shown by the SVC is noteworthy, because it does not align perfectly with that of a typical dipole source, although there are two lobes directed above and below the geometry, similar to the cylinder. This might suggest that the origin of the noise for the SVC is not purely dipolar and therefore not related to the lift fluctuations that were significantly reduced and less periodic, but still present. From literature analysis [30], it is noted that the vibrissa typically maintains a dipole directivity. Therefore, the cause was investigated within the resolution of the mesh used. A comparison was made between the simulated resolution levels for the SVC, as shown in Figure 4.28. What can be observed from comparing the two levels of mesh refinement is that the pattern for the mesh at $y^+ = 20$ is completely different from that of dipole directivity. Doubling the level of refinement, however, shows that the pattern begins to elongate along the lobes in the 90° and 180° directions, i.e., above and below the geometry, while compressing in the 0° and 180° directions, i.e., upstream and downstream. This suggests that the directivity might still be related to the phenomenon of lift fluctuations, however, because these fluctuations are significantly reduced compared to the cylinder case, a higher mesh refinement might be necessary to capture them accurately and exhibit a dipole directivity pattern. The trend suggests that this could occur if the next level of resolution is employed. An additional attempt to explain the different acoustic spectrum can be

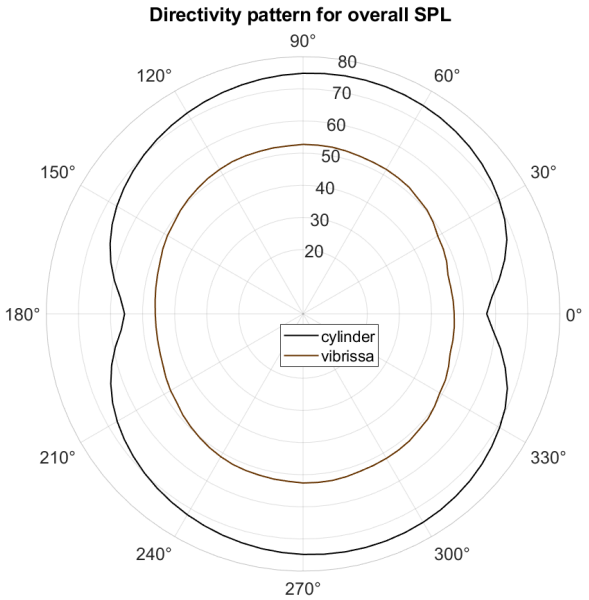

Figure 4.27: Directivity pattern for overall SPL for CC and SVC

found in the evaluation of turbulent kinetic energy (TKE). First, it is defined as:

$$\mathrm{TKE} = \frac{1}{2}\left(\overline{u'^2} + \overline{v'^2} + \overline{w'^2}\right) \tag{4.8}$$

where u', v', and w' are the fluctuating velocity components in the streamwise, longitudinal, and spanwise directions, respectively. In fact, as shown in Figure 4.26 with reduced recirculation zones for the nodal plane and in Figure 4.24 and 4.25 with the absence of coherent alternating vortices and a more stable wake area, as well as reduced lift fluctuations, it was considered to evaluate the intensity of turbulent kinetic energy (TKE), that can be associated with the level of noise for the broadband component in the spectra. As shown in Figure 4.29, the turbulent kinetic energy, non-dimensionalised with the square of the free-stream velocity, associate is significantly reduced both in spatial extent and magnitude for SVC

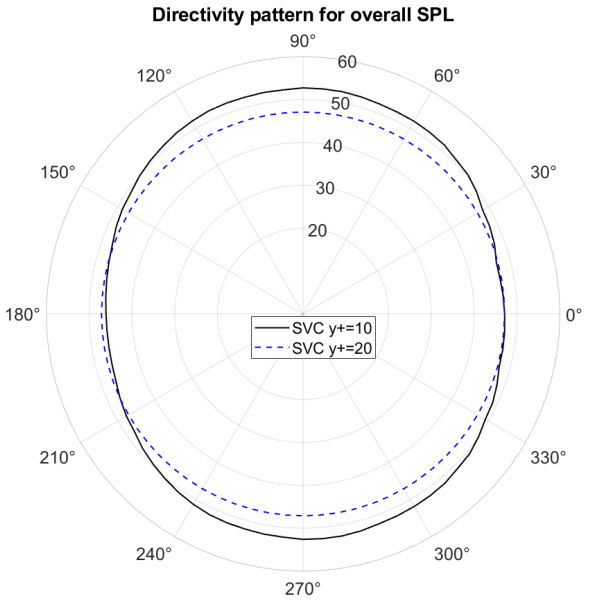

Figure 4.28: Directivity pattern for overall SPL for the SVC at different mesh resolutions

respect to the CC. It is emphasised how the scale in the comparison between CC and SVC is different. In fact, due to the reduced turbulent activity, it was necessary to decrease the maximum value in order to visualise the zones with higher activity. The results presented indicate that the significant change occurs more prominently for the nodal plane compared to the saddle plane, suggesting that this plane contributes significantly to the alteration in fluid dynamics and noise reduction. Therefore, it is relevant to examine the 3D motion introduced by the undulatory geometry of the SVC. In Figure 4.30, the time-averaged streamwise velocity in the x-z plane with streamlines illustrates this motion near the SVC, which is entirely absent for the CC. What is observed is a spanwise motion from the saddle plane to the adjacent nodal plane [15]. Additionally, the separation point follows the undulatory motion of the trailing edge, and the recirculation zone downstream is more extended for the saddle plane. However, it is evident that the recovery of the free-stream velocity occurs much faster for the SVC than for the CC. One possible interpretation is the inability to form coherent, alternating vortices given their distortion in the span direction from 3D motion and the fact that they are probably weaker given the more stable recirculation zones. A better visualisation of that can be seen in Figure 4.31 and in Figure 4.32. In the figures, it is possible to observe a different movement of the vortical structures downstream of the geometries. By combining what is shown n Figure 4.31 and in Figure 4.32 for the SVC, it is possible to interpret the movement of the vortical structures. In fact, it can be seen that the spanwise component of the velocity is alternated along the span, indicating a movement of some vortical structures towards the adjacent ones in the positive z direction, while others move in the opposite direction, meeting each other. Furthermore, these structures also exhibit different longitudinal velocities; in fact, alternately between the saddle plane and the nodal plane, they reverse their direction along the span. This movement is entirely absent for the CC.

A search for the formation of uncorrelated structures emitted from above and below the geometries involved analysing the correlation of pressure fluctuations at $\theta = 60°$ and $\theta = 300°$ along the CC and SVC, with $\theta = 0°$ being the fully downstream point. For the CC, a correlation value of -0.80 was found, whereas for the SVC, a value of 0.30 was observed in the nodal plane and 0.04 in the saddle plane [30].

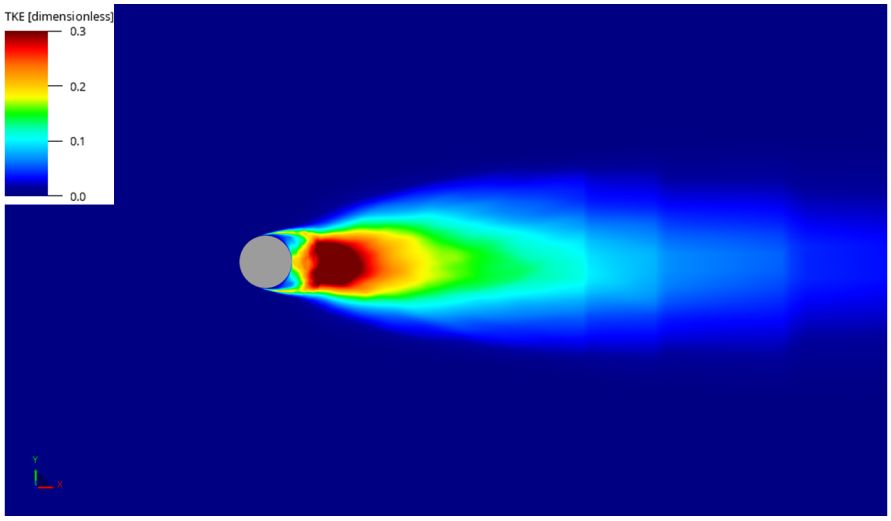

(a) CC

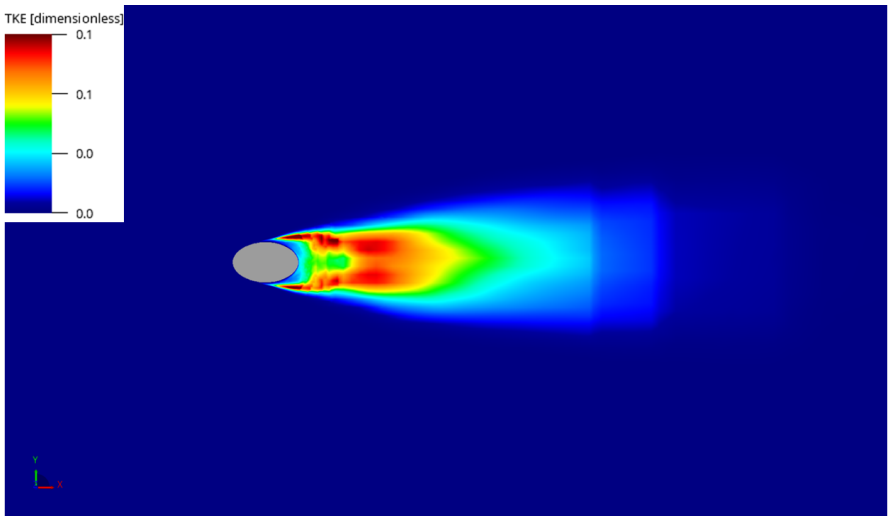

(b) SVC saddle plane

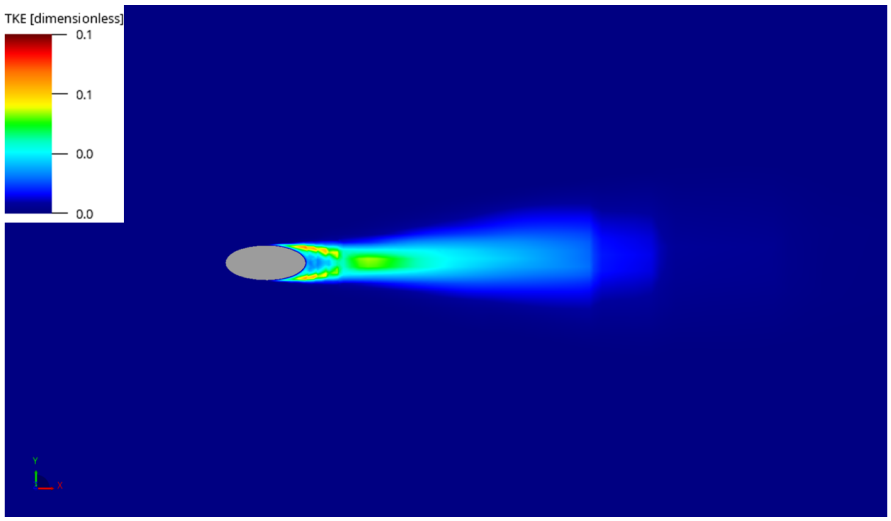

(c) SVC nodal plane

Figure 4.29: Turbulent kinetic energy

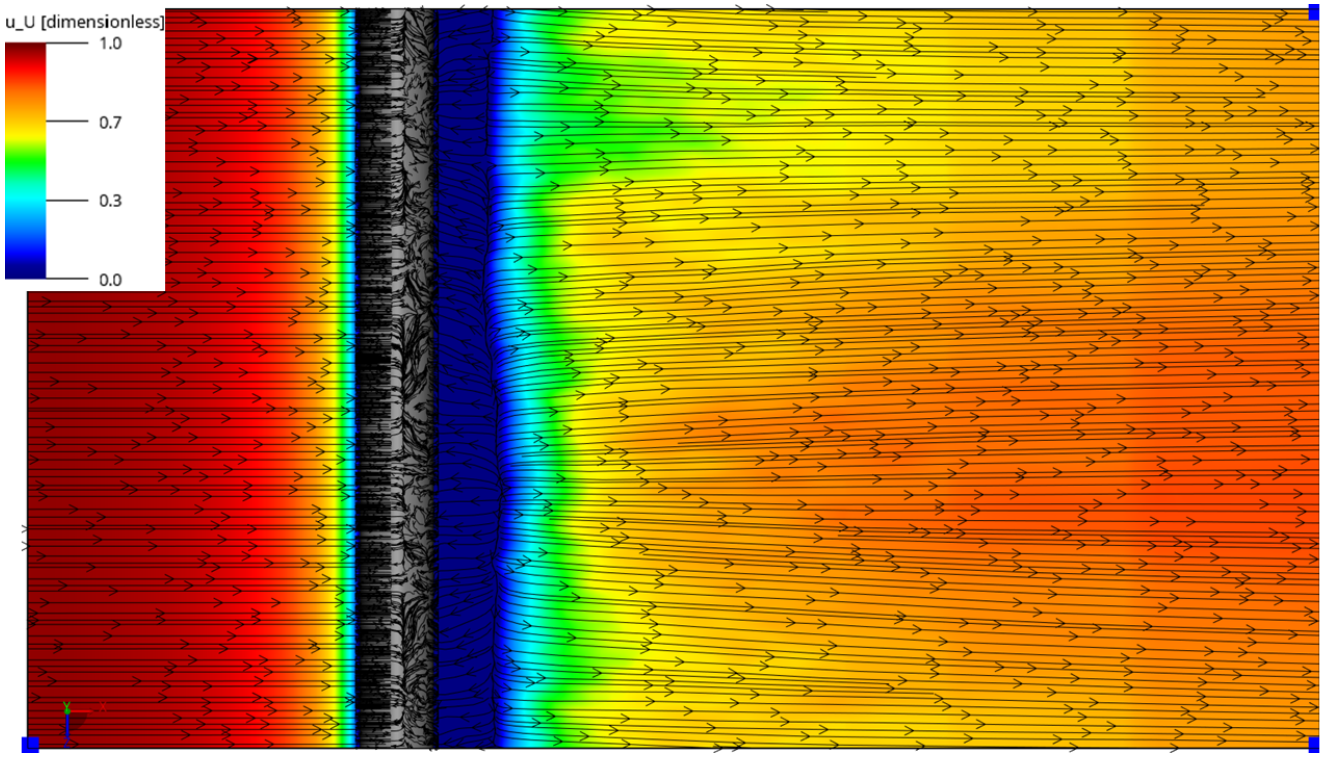

(a) CC

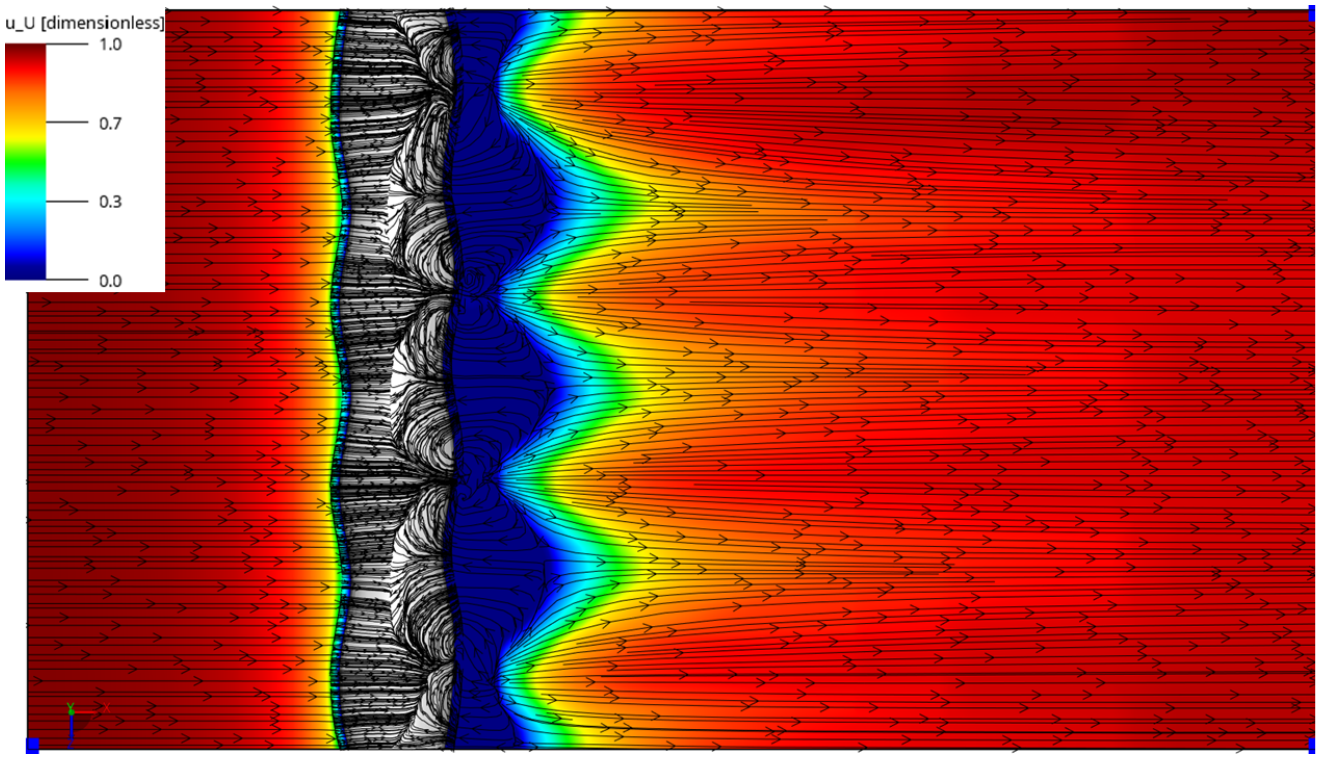

(b) SVC

Figure 4.30: Distribution of time-averaged velocity vectors and contour plot of the streamwise velocity component in the vertical plane (x-z)

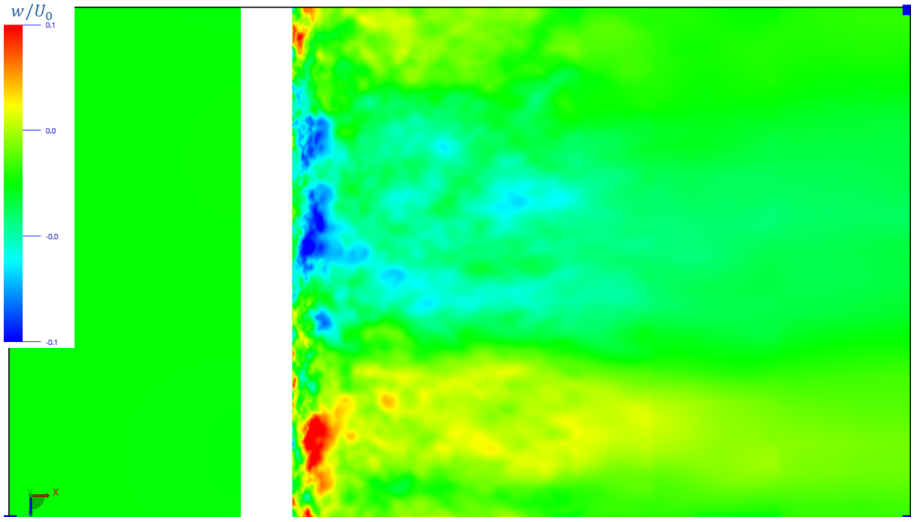

(a) CC

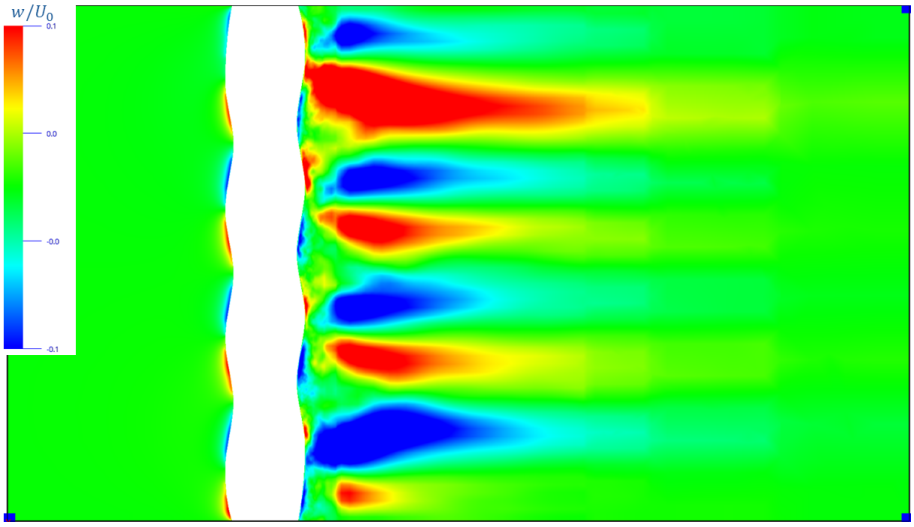

(b) SVC

Figure 4.31: Time-averaged spanwise velocity in a x-z plane

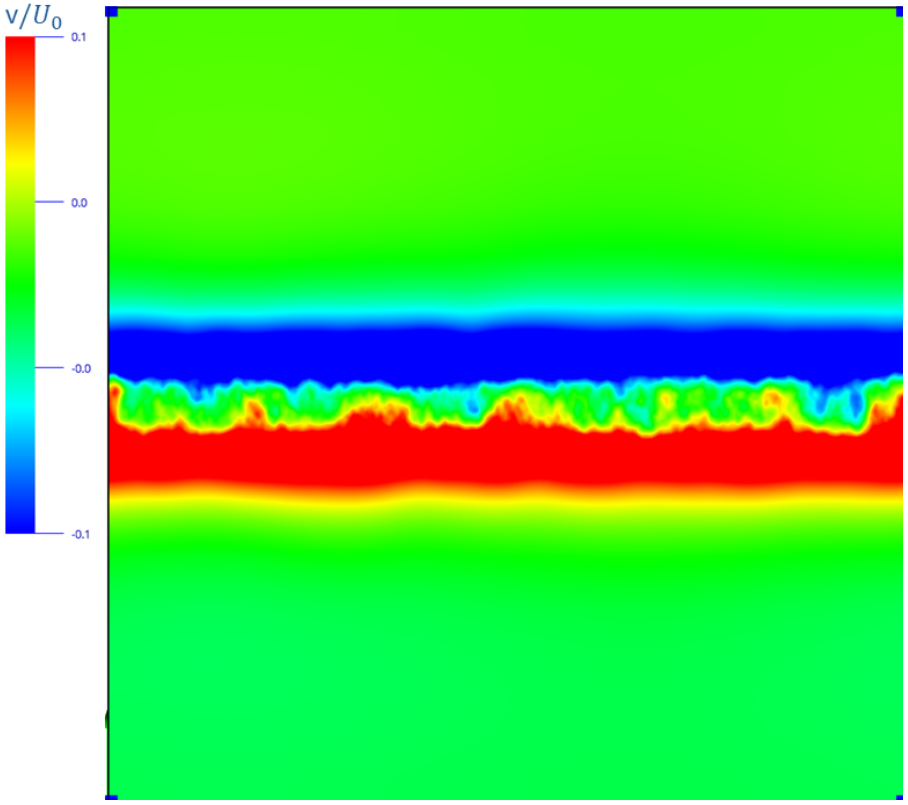

(a) CC

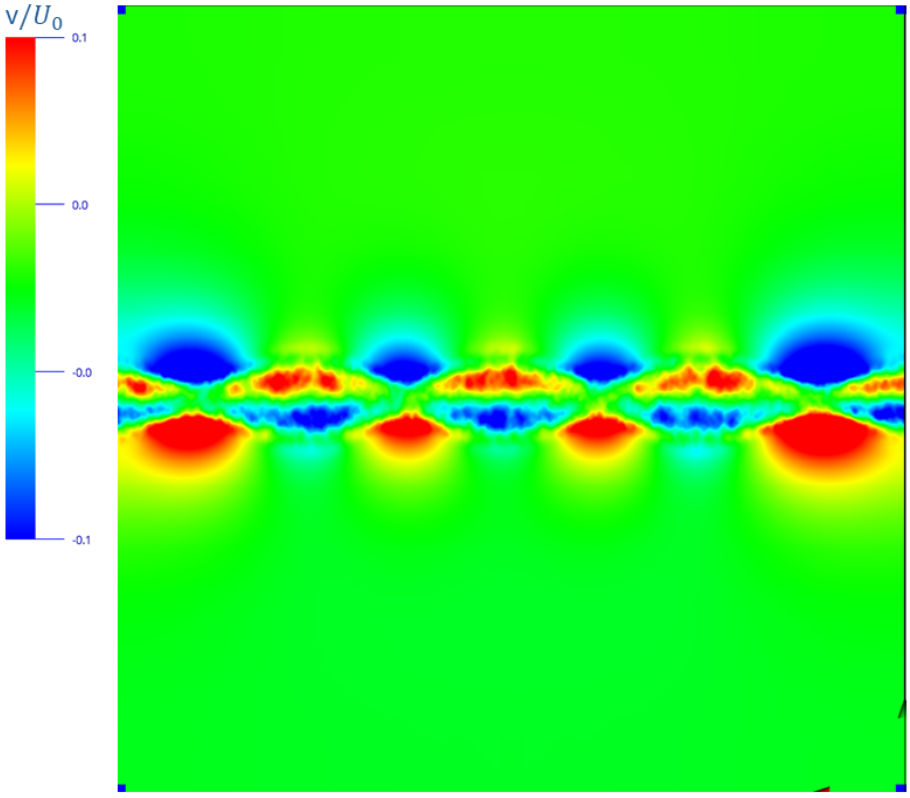

(b) SVC

Figure 4.32: Time-averaged longitudinal velocity in a y-z plane at 0.02 m downstream the geometries

Additionally, the correlation in the spanwise direction was investigated through the calculation of the correlation length to explain the absence of a narrowband component in the acoustic spectrum. The correlation length, in Figure 4.33, was evaluated by measuring the pressure over time at 801 points along the span of the two geometries, at a point 60° considering 0° as the downstream point. For the SVC, the point was set at 60° relative to the saddle plane. From the time-pressure vectors, the temporal fluctuations were obtained, and these were used to calculate the correlation length using the following formula; a similar expression has been used in the reference paper [30]:

$$R_\xi = \frac{1}{N}\sum_{i=1}^{N} \frac{\overline{p'(z_i)\cdot p'(z_i+\xi)}}{p_{rms}(z_i)p_{rms}(z_i+\xi)} \tag{4.9}$$

where $\xi = |z_i - z_j|$ is the separation distance, with z_i being the starting location and p_{rms} denotes the rms of the pressure fluctuations. Therefore, 801 curves were evaluated and then averaged. Comparing

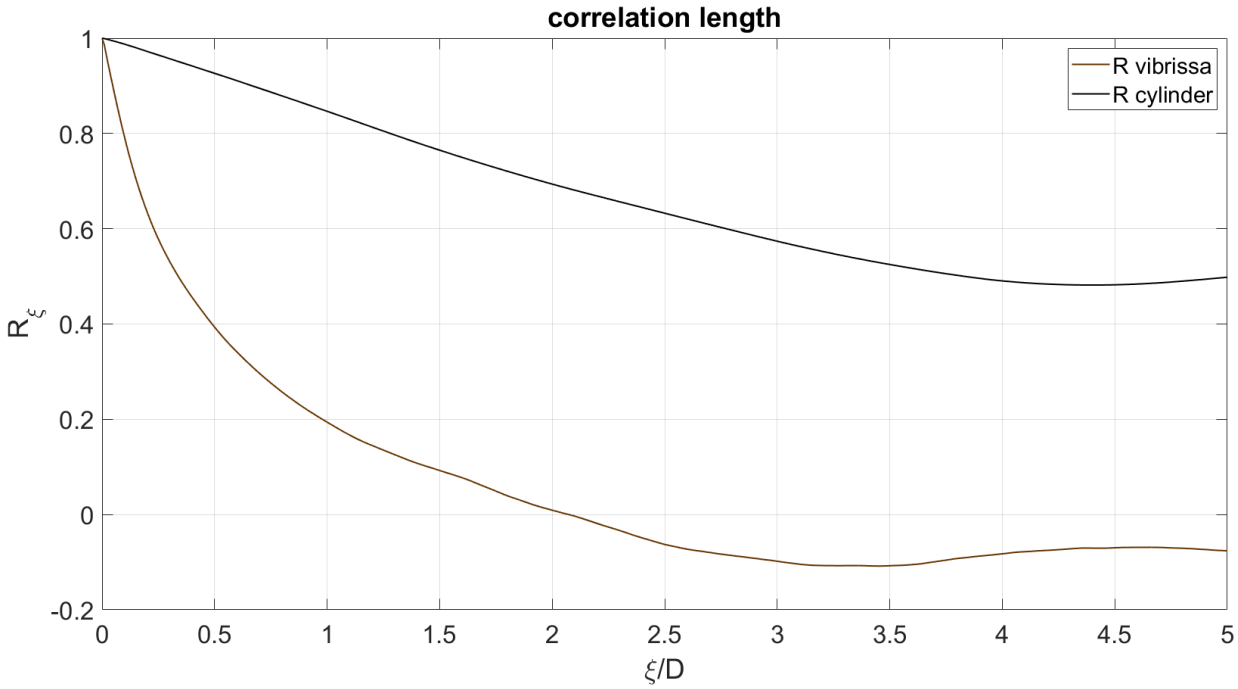

Figure 4.33: Correlation length for CC and SVC

the correlation lengths for the two geometries reveals a completely different behaviour. Specifically, the correlation of pressure fluctuations along the span for the SVC halves around $0.5D$, whereas for the CC, this loss of correlation does not occur; thus, this result in the two geometries acting as different acoustic sources.

In conclusion, in addition to the directional analysis for overall SPL (shown in Figure 4.27), the noise level was evaluated along with its propagation in the far field. Starting from the 90° point, i.e., 1.75 m above the midspan of the geometries, further distances from the geometry in that direction were assessed. As depicted in Figure 4.34, it is evident that the trend is characterised by similar curves, likely due to the nature of acoustic pressure fluctuations travelling before dissipating over long cycles. As expected, the SVC consistently maintains lower overall SPL values, reaching approximately 10 dB beyond 100 meters, while the CC stabilises at around 40 dB at the same distance. In conclusion of the study, it is highlighted that the distinct aerodynamic noise formation of a Vibrissa-Shaped Cylinder (SVC) compared to a bluff body

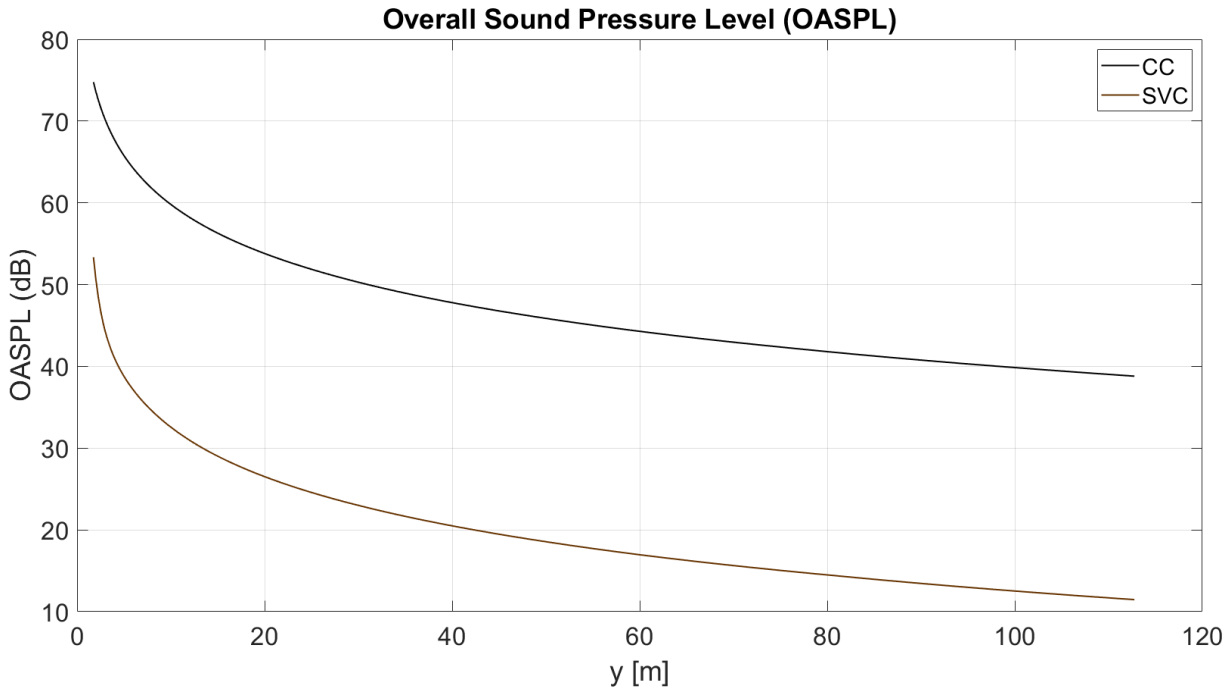

Figure 4.34: Overall SPL in the far-field

like the Circular Cylinder has been confirmed and validated. The SVC exhibits reduced and uncorrelated lift fluctuations, associated with a different wake pattern that does not lead to the generation of coherent vortices typical of vortex shedding. This difference is evident in the acoustic spectrum, which lacks tonal peaks and exhibits lower overall noise levels, as well as consistently reduced noise levels in all directions. Furthermore, this study demonstrates that the noise generated by the SVC travels into the far field while maintaining significantly lower noise levels compared to the Circular Cylinder (CC). The noise dissipates earlier due to its lower initial noise level. This could be a significant advantage for potential applications, for example in aircraft landing gear as suggested by *Smith*, *Chen*, and *Zang* [30], despite the substantial distances from the geometry, specifically beyond 100 meters.

Bibliography

[1] Anwar Ahmed and Byram Bays-Muchmore. Transverse flow over a wavy cylinder. *Physics of Fluids A: Fluid Dynamics*, 4(9):1959–1967, 09 1992.

[2] H. L. Bai, B. Zang, and T. H. New. The near wake of a sinusoidal wavy cylinder with a large spanwise wavelength using time-resolved particle image velocimetry. *Experiments in Fluids*, 2018.

[3] H.L. Bai, M.M. Alam, N. Gao, and Y.F. Lin. The near wake of sinusoidal wavy cylinders: Three-dimensional pod analyses. *International Journal of Heat and Fluid Flow*, 75:256–277, 2019.

[4] R.D. Blevins. Review of sound induced by vortex shedding from cylinders. *Journal of Sound and Vibration*, 92(4):455–470, 1984.

[5] Guanjiang Chen, Xiao Liu, B. Zang, and Mahdi Azarpeyvand. The effect of the vibrissa shaped cylinder on the aeolian tone mitigation. In *Proceedings: Internoise 2022*, pages 1–8. Institute of Noise Control Engineering, aug 2022. 51st International Congress and Exposition on Noise Control Engineering , Inter.noise 2022 ; Conference date: 21-08-2022 Through 24-08-2022.

[6] Shijun Chu, Chao Xia, Hanfeng Wang, Yajun Fan, and Zhigang Yang. Three-dimensional spectral proper orthogonal decomposition analyses of the turbulent flow around a seal-vibrissa-shaped cylinder. *Physics of Fluids*, 33(2):025106, 02 2021.

[7] N. Curle and Michael James Lighthill. The influence of solid boundaries upon aerodynamic sound. *Proceedings of the Royal Society of London. Series A. Mathematical and Physical Sciences*, 231(1187):505–514, 1955.

[8] Sumner David. *Circular cylinders in cross-flow*. PhD thesis, McGill University, Montréal, Canada, January 1999. Doctor of Philosophy in Mechanical Engineering.

[9] B. Etkin, G. K. Korbacher, and R. T. Keefe. Acoustic Radiation from a Stationary Cylinder in a Fluid Stream (Aeolian Tones). *The Journal of the Acoustical Society of America*, 29(1):30–36, 01 1957.

[10] The european parliament and the council of the european union. Regulation (eu) no 598/2014 of the european parliament and of the council of 16 april 2014. Technical report, Official Journal of the European Union, 2014.

[11] Uwe Fey, Michael König, and Helmut Eckelmann. A new Strouhal–Reynolds-number relationship for the circular cylinder in the range 47
lt;Re
lt;2×105. *Physics of Fluids*, 10(7):1547–1549, 07 1998.

[12] Hajime Fujita. The characteristics of the aeolian tone radiated from two-dimensional cylinders. *Fluid Dynamics Research*, 42(1):015002, jan 2010.

[13] Wolf Hanke, Matthias Witte, Lars Miersch, Martin Brede, Johannes Oeffner, Mark Michael, Frederike Hanke, Alfred Leder, and Guido Dehnhardt. Harbor seal vibrissa morphology suppresses vortex-induced vibrations. *Journal of Experimental Biology*, 213(15):2665–2672, 08 2010.

[14] Xiaoyi He and Li-Shi Luo. Theory of the lattice boltzmann method: From the boltzmann equation to the lattice boltzmann equation. *Phys. Rev. E*, 56:6811–6817, Dec 1997.

[15] Hongen Jie and Ying Zheng Liu. Large eddy simulation and proper orthogonality decomposition of turbulent flow around a vibrissa-shaped cylinder. *International Journal of Heat and Fluid Flow*, 67:261–277, 2017.

[16] Shigehiko Kaneko, Tomomichi Nakamura, Fumio Inada, and Minoru Kato. *Flow-Induced Vibrations: Classifications and Lessons from Practical Experiences*. Elsevier, 2008.

[17] Nikolaos D. Katopodes. Chapter 5 - viscous fluid flow. In Nikolaos D. Katopodes, editor, *Free-Surface Flow*, pages 324–426. Butterworth-Heinemann, 2019.

[18] L. S. G. Kovásznay and Geoffrey Ingram Taylor. Hot-wire investigation of the wake behind cylinders at low reynolds numbers. *Proceedings of the Royal Society of London. Series A. Mathematical and Physical Sciences*, 198(1053):174–190, 1949.

[19] B.E. Launder and D.B. Spalding. The numerical computation of turbulent flows. *Computer Methods in Applied Mechanics and Engineering*, 3(2):269–289, 1974.

[20] J.H. Lienhard and Washington State University. College of Engineering. Research Division. *Synopsis of Lift, Drag, and Vortex Frequency Data for Rigid Circular Cylinders*. Bulletin (Washington State University. College of Engineering. Research Division). Technical Extension Service, Washington State University, 1966.

[21] Michael James Lighthill and Maxwell Herman Alexander Newman. On sound generated aerodynamically i. general theory. *Proceedings of the Royal Society of London. Series A. Mathematical and Physical Sciences*, 211(1107):564–587, 1952.

[22] Xiao Liu, Guanjiang Chen, B. Zang, and Mahdi Azarpeyvand. An experimental study of aeroacoustic and aerodynamic performance of the wavy and vibrissa shaped cylinders. In *28th AIAA/CEAS Aeroacoustics Conference, 2022*, 28th AIAA/CEAS Aeroacoustics Conference, 2022, pages 1–15, United States, June 2022. American Institute of Aeronautics and Astronautics Inc. (AIAA). Funding Information: The second author is funded by the China Scholarship Council (CSC)-University of Bristol (UoB) PhD Scholarship. Publisher Copyright: © 2022, American Institute of Aeronautics and Astronautics Inc, AIAA. All rights reserved.

[23] A. W. Marris. A Review on Vortex Streets, Periodic Wakes, and Induced Vibration Phenomena. *Journal of Basic Engineering*, 86(2):185–193, 06 1964.

[24] Roberto Merino-Martinez, Lothar Bertsch, Dick G. Simons, and Mirjam Snellen. *Analysis of landing gear noise during approach*.

[25] O. M. Phillips. The intnesity of aeolian tones. *Journal of Fluid Mechanics*, 1(6):607–624, 1956.

[26] Y. H. Qian, D. D'Humières, and P. Lallemand. Lattice bgk models for navier-stokes equation. *Europhysics Letters*, 17(6):479, feb 1992.

[27] E G Richardson. Aeolian tones. *Proceedings of the Physical Society of London*, 36(1):153, jan 1923.

[28] Anatol Roshko. On the development of turbulent wakes from vortex streets. *UNT Digital Library*, 1954.

[29] John W. Schaefer and Salamon Eskinazi. An analysis of the vortex street generated in a viscous fluid. *Journal of Fluid Mechanics*, 6(2):241–260, 1959.

[30] Tom A. Smith, Guanjiang Chen, and Bin Zang. Aeroacoustic performance of a seal vibrissa shaped cylinder. *The Journal of the Acoustical Society of America*, 154(3):1585–1595, 09 2023.

[31] Mohamed Sukri Mat Ali, Con J. Doolan, and Vincent Wheatley. The sound generated by a square cylinder with a splitter plate at low reynolds number. *Journal of Sound and Vibration*, 330(15):3620–3635, 2011.

[32] Christopher M. Teixeira. Incorporating turbulence models into the lattice-boltzmann method. *International Journal of Modern Physics C*, 09(08):1159–1175, 1998.

[33] D. J. Tritton. Experiments on the flow past a circular cylinder at low reynolds numbers. *Journal of Fluid Mechanics*, 6(4):547–567, 1959.

[34] Shaofei Wang and Yingzheng Liu. Wake dynamics behind a seal-vibrissa-shaped cylinder: a comparative study by time-resolved particle velocimetry measurements. *Experiments in Fluids*, 57(3):1–20, 2016.

[35] Matthias Witte, Wolf Hanke, Sven Wieskotten, Lars Miersch, Martin Brede, Guido Dehnhardt, and Alfred Leder. *On the Wake Flow Dynamics behind Harbor Seal Vibrissae – A Fluid Mechanical Explanation for an Extraordinary Capability*, pages 271–289. Springer Berlin Heidelberg, Berlin, Heidelberg, 2012.

[36] Victor Yakhot and Steven A. Orszag. Renormalization-group analysis of turbulence. *Phys. Rev. Lett.*, 57:1722–1724, Oct 1986.